I give permission for public access to my thesis for any copying to be done at the discretion of the archives librarian and/or the College librarian.

Signature Date

ABSTRACT

Understanding the morphology of volcanic features on the Moon is essential to discovering their emplacement mechanisms. Terrestrial lava flows were previously studied using radar imaging in an attempt to distinguish differing flow morphologies – SIR-B radar data taken over Kilauea Volcano in Hawaii have shown it is possible to distinguish rough a'a features from smoother pahoehoe flows, as well as pyroclastic ash (Gaddis et al., 1989). With these observations, it is likewise possible to use radar to distinguish different volcanic terrains on the Moon. Rugged lava flows on the Moon such as that in Mare Serenitatis have been identified using Earth-based radar, and by observing areas of high circular polarization ratio (CPR) it is possible to infer their original flow morphologies (Campbell et al., 2009a).

Ground-based radar has likewise been used to identify pyroclastic deposits by their low CPR values in Mare Vaporum and Mare Serenitatis (Carter et al., 2009). In this work, we explore the relationship between surface roughness and the radar signatures of various lunar volcanic domes, as well as other lunar geologic features. In order to quantify this relationship, we compared radar CPR values at S- and P-band wavelengths (12.6 and 70 cm, respectively) with pulse width and RMS topographic roughness attained from LOLA data. The comparison of these different parameters describes surface roughness on a range of length scales.

Several regions on the Moon were analyzed using this technique: volcanic domes include the Marius Hills, the Gruithuisen and Mairan domes, as well as the Rümker Hills; other features analyzed include various mare lava flows, dark mantle deposits, and two young craters.

THE RELATIONSHIP BETWEEN RADAR SCATTERING AND LUNAR SURFACE ROUGHNESS

By
Erica Ruth Jawin

A paper presented to the Department
of Astronomy of Mount Holyoke College
in Partial Fulfillment of the Requirements
for the Degree of Bachelors of Arts with Honor

Advisors: Darby Dyar, Caleb Fassett

Department of Astronomy
South Hadley, MA 01075

May 2012

ACKNOWLEDGEMENTS

This project started as a summer internship, so it is only natural to start my acknowledgements there. I'd like to firstly thank the Lunar and Planetary Institute for the fantastic internship this past summer. I am forever grateful to Walter Kiefer, my advisor at LPI, for designing this project and guiding me through this summer (and throughout the year), as well as teaching me the art of "creative floundering" – a skill that will likely prove useful in coming years. Paul Spudis also deserves my thanks for being a fantastic co-advisor and reliable resource on all things radar.

My fearless "unofficial" thesis advisor, Caleb Fassett, deserves more thanks than I can give him, for taking my thesis and me on in his first year at Mount Holyoke. He may not have known what he was getting himself into, but this thesis wouldn't be what it is without his help.

It goes without saying that I thank Darby Dyar, my mentor forever (and the reason I came to Mount Holyoke). She has guided me and helped me grow in more ways than she knows. If we ever get around to making "Darby Club" T-shirts, I will wear mine with pride.

I would like to thank Mount Holyoke College for the fantastic education I've received here. The past three years have gone by quickly, and I can't imagine leaving. Also thank you to my third committee member, Michelle Markley, for leaving Earth for a brief time to come study the geology of the Moon.

Thank you thank you thank you to my friends, especially Julia, Julita and Paige. You made it all manageable, even when it seemed like it couldn't be done.

Many thanks to Thirsty Mind for staying open late on weekdays. I should also thank Pandora Radio – my Sleigh Bells station, with its "hard rock roots, electronic influences, hip-hop influences, r & b influences, and punk influences", made endless hours of data collection, text formatting, and editing manageable.

Finally, I of course have to thank my family. Mom, Dad, Rachel, Tom, and (especially this year) Ali, thank you for supporting me through everything. None of this would be possible without your love and inspiration. And thank you to Sasha. For everything, always.

TABLE OF CONTENTS

TABLE OF CHARTS/FIGURES

INTRODUCTION

It is a very beautiful thing, and most gratifying to the sight, to behold the body of the moon… one may learn with all certainty of sense evidence that the moon is not robed in a smooth and polished surface but is in fact rough and uneven, covered everywhere, just like the earth's surface, with huge prominences, deep valleys, and chasms. (Galilei, 1957, p. 27-28)

Galileo's *The Starry Messenger,* along with the introduction of the telescope in the early 17th Century, aided in revolutionizing observational astronomy. Long before this time, however, humans spent countless hours studying the Moon's surface; it was only after the advent of new technologies such as the telescope that it became possible to view the surface of the Moon with unparalleled clarity. As technology advanced, we developed new techniques of studying celestial bodies, such as the placement of artificial satellites in orbits around the Moon and other planets, and the exploration of other planets by landers, rovers, and for a brief time, humans. These have contributed to the collective understanding of how our Solar System formed and evolved. These

advances allowed us to introduce new technologies such as spectroscopy, laser ranging, and radar, which enabled generations of future scientific discoveries.

The Moon remains the only body other than Earth that humans have visited. Partially because of this, the Moon is the most explored body in our solar system (after Earth). This is primarily due to the proximity of the Moon to Earth, as well as the paucity of a lunar atmosphere. Despite this record of exploration and centuries of research, many aspects of the Moon remain enigmatic.

Studying the morphological characteristics of lunar geologic features is integral to understanding certain aspects of the Moon's geologic history. Likewise, the interaction between the lunar exterior and its space environment leads to the evolution of the lunar surface over time. Characteristics such as composition, age, and emplacement mechanisms can all affect a feature's physical appearance. One measurement that can be used to characterize this is surface roughness. This thesis focuses on quantifying the roughness of various lunar geologic features. Surface roughness in this work follows the definition given by Campbell & Shepard (1996), "the [variation in] topography of natural surfaces at scales

of a few meters or less" (p. 18,941). Roughness can be manifested on various length scales: large-scale features include topographic variation, while smaller-scale heterogeneity can result from meter-scale boulders to centimeter-scale pebbles. In this study, roughness measurements were gathered using a combination of remote sensing techniques, namely laser altimetry and radar.

The laser altimetry measurements in this thesis were collected using the Lunar Orbiter Laser Altimeter (LOLA) on the Lunar Reconnaissance Orbiter (LRO) (Smith et al., 2010b). Because of LOLA's incredible vertical precision of 10 cm (compared to the Mars Orbiter Laser Altimeter's vertical precision of ~1.5 m) (Smith et al., 2001), the surface roughness calculations detailed here are orders of magnitude better than previous work. Radar data at the S-band wavelength (12.6 cm) from the Mini-RF (Miniature-Radio Frequency) instrument, also on LRO (Nozette et al., 2010), as well as the P-band wavelength (70 cm) from the Earth-based Arecibo Telescope (Campbell et al., 2009b), are compared against the altimetry data. The radar data in this project are in the form of circular polarization ratio (CPR), which is a measure of radar scattering (Nozette et al., 2010).

1.1 Why Radar?

Radar has proven to be extremely useful in identifying and distinguishing geologic features, both on Earth and on other astronomical bodies. This is due in large part to a correlation between surface roughness and radar scattering, which will be described fully in the following chapter. Comparative measurements taken of Kilauea Volcano in Hawaii using Space Shuttle Imaging Radar (SIR-B) showed volcanic formations of differing textures, namely a'a and pahoehoe flows, as well as pyroclastic ash deposits, were distinguishable at the L-band (23 cm) wavelength (Gaddis et al., 1990). Additionally, Earth-based P-band (70 cm) radar proved useful in identifying rugged lava flows on the Moon, such as that in Mare Serenitatis (Campbell et al., 2009a), while S-band (12.6 cm) data were used to identify fine-grained pyroclastic deposits by their low backscatter and CPR values in Mare Vaporum and southern Mare Serenitatis (Carter et al., 2009). Radar plays a key role in this thesis project because of its wide array of applications, as well as the variety of features it can help to identify.

1.2 Objectives for the project

This thesis encompasses many geologic features across the lunar nearside. However, the inspiration for the project originated from a distinct roughness signature in one specific area: Campbell et al. (2009b) used ground-based P-band radar to study volcanic domes in the Marius Hills Complex in Oceanus Procellarum. Their results showed that the domes demonstrated markedly higher circular polarization ratio values compared to the surrounding mare (Figure 1). This thesis uses higher resolution radar data from Mini-RF, as well as the ground-based radar used by Campbell et al. (2009b), to better understand and quantify this distinct radar signature of the Marius Hills domes. These data are then compared to data obtained from laser altimetry. This comparison will yield surface roughness measurements on a range of length scales.

In addition, this technique was applied to several features of varying characteristic surface roughnesses. In addition to the Marius Hills domes, other dome units analyzed include the Gruithuisen and Mairan domes, as well as regions of the Rümker Hills. Additionally, smooth and

rough end-member features were analyzed as a comparison against the lunar domes. The smooth features that were examined include mare flows in Imbrium, Oceanus Procellarum and regions of the Marius Hills plains; additional smooth features include various regions of pyroclastic dark mantle deposits. Conversely, the rough lunar features that were analyzed include two young craters, Copernicus and Tycho. These craters were analyzed on both the ejecta blankets surrounding the crater, and impact melt sheets on the crater floors.

As an additional experiment, this technique of comparing radar to laser altimetry was then applied to mare basalts of varying ages. Because crater density, as well as regolith depth, increases with age (Langevin & Arnold, 1977; Hiesinger et al., 2000), the surface roughness of lava flows may be diagnostic of these changes. In light of this, we apply our method of measuring surface roughness to various mare basalts according to ages assigned by Hiesinger et al. (2000; 2003; 2010) in an attempt to understand the evolution of mare surface roughness over time. By comparing laser altimetry data and measured radar scattering, it is possible to acquire precise, quantitative values for surface roughness at a range of length scales.

BACKGROUND

2.1 GEOLOGIC FEATURES

2.1.1 Volcanic Domes

A variety of volcanic domes were analyzed for this study, encompassing a range of sizes and locations across the lunar surface. This range of features was intentionally selected for the purpose of determining how surface roughness characteristics are affected by different emplacement mechanisms, compositions, and ages. These dome units include: Marius Hills domes; Gruithuisen domes; Mairan domes; and the Rümker Hills complex. The following provides a detailed discussion about the morphology, composition and justification for analysis of these dome units.

2.1.1.1 Volcanic Domes: Marius Hills Domes

The Marius Hills Complex (MHC) contains the highest concentration of volcanic domes on the Moon. This region spans 35,000

km^2 and is located on a 100-200 m-high plateau in Oceanus Procellarum (Figure 2) (Weitz & Head, 1999). In addition to over 200 domes of varying sizes, the MHC also exhibits other geologic features including volcanic cones, rilles and lava flows, indicating volcanic activity was varied and complex in this region (Besse et al., 2011).

The Marius Hills yielded evidence for two distinct compositional units when analyzed using Galileo multispectral imaging by Sunshine et al. (1994). Clementine UV/VIS spectroscopy was later applied to study the MHC, using five spectral channels between 415 and 1000 nm (Weitz & Head, 1999). After studying the region, Weitz & Head (1999) concluded that the complex was composed of two mare units, high- and low-titanium basalt, with mixed boundaries. Additionally, Weitz & Head (1999) interpreted the domes as having the same composition as the surrounding mare.

Besse et al. (2011) reanalyzed this area using the Moon Mineralogy Mapper (M^3), an instrument aboard the Indian Space Research Organization's (ISRO) Chandrayaan-1 spacecraft. M^3 provided much higher spatial and spectral resolution than previous instruments; while Clementine UV/VIS data consisted of five spectral channels between 0.415

and 1 μm, M^3 used 85 channels between 0.43 and 2.97 μm (Besse et al., 2011). These detailed measurements allowed Besse et al. (2011), like Sunshine et al. (1994) and Weitz & Head (1999), to conclude that the MHC was composed of two distinct mare units. However, the M^3 data suggested that these include a high-calcium pyroxene mare and an olivine-rich mare (Figure 3), while the domes exhibit the same composition as the pyroxene-rich unit. Additionally, in some areas the olivine-rich mare embays the domes, leading to the conclusion that the olivine-rich flows are younger than the high-calcium pyroxene flows and domes (Besse et al., 2011).

Because the domes display similar spectra to other high-calcium pyroxene maria, it is possible that they formed from a melt of the same composition. It is not clear what caused the large-scale morphologies of the low-and steep-sided domes as opposed to the smooth mare flows, given that the dome morphology is likely the result of a more viscous magma. Several processes can cause this increase in viscosity, including increased silica content, lowered magma temperature, and higher crystal content (Weitz & Head, 1999). Because the composition of the domes is known to agree with the mare unit, it is unlikely the magma was more

evolved. An alternative hypothesis is that the domes are a result of lower eruption temperatures (and higher crystal content), generally occurring in magmas near the final stages of eruption. Weitz and Head (1999) therefore posit that the domes in the Marius Hills most likely resulted from magmas erupting during the terminal phases of eruption of the maria in this region.

In addition to the spectral analyses of the Marius Hills Complex with data from Galileo SSI, Clementine, and M^3, Campbell et al. (2009b) analyzed the MHC using S- and P-band (12.6 and 70 cm) wavelength ground-based radar, analyzing both radar backscatter and circular polarization ratio (CPR). CPR, which will be discussed at length later in this chapter, provides a means of studying the extent of diffuse scattering by wavelength-scale features, or spectral scattering on features that are smooth on the scale of the wavelength (Campbell et al., 2009b). Results of this study (Figure 1) found the CPR of the domes was significantly higher (0.48-0.91 in P-band) than in the surrounding mare (0.2-0.4), while the dome CPR values were considerably larger in 70 cm radar than in 12.6 cm. Campbell et al. (2009b) used these observations to conclude that these higher values occur due to either greater near-surface rock abundance or

rougher terrain on the domes, as opposed to typical mare lava flows, and postulate, like Weitz & Head (1999), that the domes must have formed from a magma with either an evolved composition, cooling effect, or variable effusion rate, or some combination of the three.

The Marius Hills Complex clearly exhibited complicated volcanic activity throughout its formation. The surface roughness of the Marius Hills domes and plains on different length scales may therefore reveal new information about the emplacement mechanisms of the Marius Hills Complex as a whole.

2.1.1.2 Volcanic Domes: Rümker Hills Complex

The Rümker Hills Complex (referred to as Mons Rümker in Campbell et al., 2009b) is a volcanic region with a diameter of 80 km containing over 30 coalesced domes in northern Oceanus Procellarum (Weitz & Head, 1999) (see Figure 4). Clementine spectra of the region show the domes are indistinguishable from the surrounding mare (Figure 5), and are of similar composition to the Marius Hills domes (Weitz & Head, 1999). However, the domes in this complex appear flat compared to

those in the Marius Hills, potentially reflecting diverse emplacement mechanisms across the two regions.

Despite compositional similarities, Campbell et al. (2009b) observed very different radar signatures in the Rümker Hills compared to the Marius Hills; indeed, radar properties of the Rümker Hills appear more similar to those of the Aristarchus Plateau. Circular polarization ratio values for this region at S-band (12.6 cm wavelength) (Figure 6A) were generally lower than the surrounding mare. As a comparison, P-band (70 cm wavelength) data (Figure 6B) were very low in the northern region and to a lesser extent the southern region, but showed a band of moderate to high CPR values in the north-central region (Campbell et al., 2009b).

These low radar CPR signatures at both S- and P-band wavelengths suggest a very small population of rocks larger than ~2 cm in diameter in the uppermost meter or two, as well as a paucity of decimeter-diameter and larger rocks in the upper 5-10 m of the Rümker Hills (Campbell et al., 2009b). Campbell et al. (2009b) conclude that, based on these data, the northernmost section of the Rümker Hills (if not the entire complex), "…is mantled by several meters of fine-grained, rock-poor material of basaltic composition… A pyroclastic origin, similar to that of thick mantling units

on the Aristarchus Plateau, seems most likely." This basaltic mantle could, however, be overlying a core composed of highlands material – Weitz & Head (1999) observed a much higher spectral return from small craters in the northern region (Figure 5, see "Crater Wall" unit). These returns, they believe, occurred due to exposed highlands materials. This signature agrees with the CPR data (Campbell et al., 2009b), especially at 70 cm wavelength (Figure 6B).

Because the Rümker Hills exhibit a complex morphology, they provide an exceptional test subject for this project. Additionally, their similar composition to the Marius Hills offers a good basis for comparison, since their interpreted pyroclastic origin may help differentiate effects that relate to composition and emplacement style.

2.1.1.3 Volcanic Domes: Gruithuisen and Mairan Domes

Two other volcanic dome units were analyzed in this project – the Gruithuisen and Mairan domes (Figure 4). These large, steep-sided domes are morphologically and spectrally distinctive from both the Marius Hills and the Rümker Hills domes, and are believed to have formed from silicic or viscous magma (Weitz & Head, 1999; Wilson & Head, 2003; Glotch et

al., 2010). Weitz & Head (1999) used Clementine multispectral data to analyze these two sets of domes – spectrally the Mairan domes appear red, similar to the highland material to the east (Figure 7); the Gruithuisen domes also appear red when compared to the highlands. Additionally, spectra of the domes (Figure 8) show much higher albedo than typical basaltic material, similar to feldspathic material and the lunar highlands (Weitz & Head, 1999). This reasoning led Weitz & Head (1999) to conclude that the Gruithuisen and Mairan domes are most likely composed of nonmare material, similar yet spectrally distinct from that of the highlands. Wilson & Head (2003) agree with this sentiment and state that these domes likely formed from extremely viscous melts, similar to terrestrial melts that form rhyolites, dacites and basaltic andesites. Glotch et al. (2010) analyzed spectra of the Gruithuisen domes as well, using data from the Diviner Lunar Radiometer Experiment (DLRE) onboard the Lunar Reconnaissance Orbiter (LRO). They concluded that the spectra of these domes suggest a silicic, extrusive volcanic origin.

Both the Gruithuisen and Mairan domes contain compositional idiosyncrasies. While the Rümker Hills are compositionally similar to the Marius Hills, the Gruithuisen and Mairan domes are potentially more

silicic. Terrestrial silicic lava domes are well studied using radar, and are known to be extremely rough; Plaut et al. (2004) found silicic dome surfaces to be "among the roughest ever measured." Circular polarization ratio measurements were observed for terrestrial silicic domes between 0.3-0.95 depending on wavelength, with longer wavelengths yielding higher CPR values. The relatively silicic composition of both the Gruithuisen and Mairan domes are thus expected to show high CPR values, and provide an upper limit for dome surface roughness.

2.1.2 Lava Flows

In addition to the relatively rough volcanic domes, lava flows that represent more typical expressions of mare volcanism were also measured. These flows provide a smoother surface for analysis. For this reason, various mare units were analyzed based on their location and terrain.

2.1.2.1 Lava Flows: Smooth Mare Flows

Campbell et al. (2009b) discovered the plains of the Marius Hills had much lower CPR values than the domes themselves (Figure 1D). To confirm and quantify this relationship, regions of the mare plains between

volcanic domes (see Figure 2) were analyzed in the Marius Hills. In addition to this region, other mare flows include regions of Oceanus Procellarum and Mare Imbrium.

These smooth mare lava flows may be akin to terrestrial pahoehoe flows. These smooth, ropy basaltic formations likewise yield low radar returns; Gaddis et al. (1990) distinguished various volcanic terrains, including assorted pahoehoe flows, on Kilauea Volcano in Hawaii using Space Shuttle Imaging Radar (SIR-B). Additionally, circular polarization ratio values for Hawaiian pahoehoe have been constrained between 0.15-0.4 (Plaut et al., 2004). The smooth mare flows of the Marius Hills plains, Oceanus Procellarum and Mare Imbrium should likewise be distinguishable by their low CPR values.

2.1.2.2 Lava Flows: Rough Mare Flows

The analysis of rugged maria provided an upper limit for lava flow surface roughness. As smooth mare flows were likened to pahoehoe flows above, rougher flows may be analogous to terrestrial a'a. These rough, blocky Hawaiian basalts have yielded CPR values between 0.3-0.6 (Plaut et al., 2004).

Campbell et al. (2009a) identified certain rugged mare flows that return high CPR values. These flows are located in Mare Serenitatis, Mare Imbrium and Mare Crisium. These rough flows are believed to have a greater abundance of decimeter-diameter subsurface rocks compared to other mare-forming flows, with an initial flow thickness of at least 3-5 m (Campbell et al., 2009a); despite regolith buildup, these areas still appear rugged in radar, and they provide an upper limit for mare flow roughness.

2.1.3 Dark Mantle Deposits

While rugged mare features such as those in Mare Serenitatis represent an upper limit to mare surface roughness, it would be analogously helpful to have a lower limit representing smooth volcanic features. Ideal subjects for this are pyroclastic ash deposits, similar to those found on Earth. These pyroclastic formations, known as dark mantle deposits (DMD's) are defined by Campbell et al. (2008) as, "blankets of fine-grained glass and quenched-crystal glass spheroids formed by eruptions of gas-rich magma during the early phases of the basaltic volcanism that flooded most basin floors." These DMD's generally have similar characteristics, as described by Head (1974), including: low-albedo

as compared to other units; location near upland areas adjacent to maria; smooth surfaces, suggesting mantling of underlying topography; and ages younger than the Imbrium event, but older than the most recent mare emplacement.

Multiple distinct pyroclastic eruptions have occurred that resulted in DMD's, including extremely large (over 2500 km^2) deposits; these large eruptions were likely formed from long-term fire fountaining occurring along with basaltic volcanism (Carter et al., 2009). Three of these areas were analyzed in this project: Sinus Aestuum, Sulpicius Gallus, and Mare Vaporum (Figure 9). When analyzed using radar, these pyroclastic deposits predictably had extremely low values of CPR (Figure 10), due to fine-grained volcanic material which mantled previously deposited surface material (Carter et al., 2009). These particularly low values provide an ideal lower bound for surface roughness.

2.1.4 Young Craters

Impact cratering has occurred throughout the entire history of the Moon, and crater formations control the lunar surface more than any other geologic process. Craters, particularly young craters provide ideal

samples of exceptionally rough surfaces. After an impact, a crater erodes continuously due to micrometeorite impacts and cosmic ray bombardment. As degradation occurs, regolith thickness increases, which both softens angular edges of rocks and decreases topographic variation, leading to less surface roughness (Langevin & Arnold, 1977). Young craters therefore are less degraded and are morphologically rougher than older craters. For this reason two young complex craters were studied, namely Tycho and Copernicus craters.

Two distinct areas of each crater – the crater floor, and the ejecta blanket – were analyzed in this thesis. Complex craters have relatively flat floors (as opposed to simple craters that have no central flat area and are paraboloidal in shape) (Melosh, 1989), and yet the impact melt sheets found there are extremely rough. Additionally, young complex craters like Tycho and Copernicus have well-preserved ejecta blankets, which have not yet degraded significantly. Both of these crater features represent some of the roughest terrains on the Moon.

2.1.4.1 Young Craters: Copernicus Crater

Copernicus Crater is 95 km in diameter, containing several prominent central peaks on the crater floor, as well as bright ejecta rays (Figure 11) (Pieters, 1982; Hawke et al., 2004). Additionally, the crater has been dated to ~800 x 10^6 yr (Eberhardt et al., 1972; Bogard et al., 1994), which defines the beginning of the most recent lunar time period of the same name. Much interest has focused on Copernicus Crater due to the detection of olivine in its central peaks; the lunar highlands are composed mainly of plagioclase, while peridotite that formed in the Magma Ocean sank and formed the crust or mantle (Liu et al., 2011). The material composing the central peaks of Copernicus Crater is therefore believed to have been uplifted from a depth of ~10 km through dynamic rebound after the impacting event (Pieters, 1982). Recent detections of Mg-Spinel in the central peak also are likely excavated from great depth (Dhingra & Pieters, 2011). These peaks of formerly subterranean material provide a glimpse of the lunar interior, and may originate from the upper mantle (Yamamoto et al., 2010).

2.1.4.2 Young Craters: Tycho Crater

Tycho Crater is likewise a young, complex crater with a diameter of about 85 km, and is known as one of the youngest features of its size on the Moon (Figure 12) (Pettengill & Thompson, 1968). It is easily visible from Earth, especially at the full moon, and bright rays cover approximately 560,000 km^2 (Dundas & McEwen, 2007).

Early studies of the radar properties of Tycho reveal much about its geologic characteristics. In 1968 Pettengill and Thompson analyzed Tycho Crater using ground-based 3.8 and 70 cm wavelength radar. They note that previous studies suggested enhanced radar scattering

> …was largely confined to the interior of the crater. Comparison of measurements made in the polarized and depolarized receiving modes showed that the observed enhancement could be attributed entirely to increased roughness. In addition, a "halo" showing a twofold increase in reflected power was noted which extended approximately 100 km beyond the rim in all directions except to the south. (Pettengill & Thompson, 1968 p. 458-459)

Pettengill & Thompson (1968) also discuss Tycho's "jagged surface", which is rough on both small and large scales, from a few centimeters up to tens of meters, which appears much rougher than other lunar surface features that predate Tycho.

These distinct radar signatures are expected of young craters such as Tycho and Copernicus. For this reason, these craters were analyzed both on their crater floors as well as their ejecta blankets (referred to as "halos" by Pettengill & Thompson, 1968, above) to supply larger values of surface roughness.

2.1.5 Mare Flows of Various Ages

Mare basalts cover around 17% of the lunar surface (Hiesinger et al., 2010), mostly concentrated on the lunar nearside. Maria are younger than the lunar highlands, although the volcanism that formed the mare basalts varies widely in age. Likewise, the mineralogy of mare basalts also varies with age (Hiesinger, 2000). Basin-filling volcanic activity started around 3.9-4.0 Ga, and continued until around 2.0 Ga, with a few very young flows with ages ~1.2 Ga (Hiesinger et al., 2000).

Four main methods are used to date mare basalts: laboratory radiometric investigation of returned samples; crater degradation studies; stratigraphic study of ejecta blankets; and measurement of crater size-frequency distribution (Hiesinger et al., 2000). While all are effective, Hiesinger et al. (2000; 2003; 2010) used crater size-frequency distribution

measurements to date most of the maria on the lunar nearside. This approach involves two steps: measuring the surface area of a single geologic unit; and measuring the diameters of every primary crater in that unit (Hiesinger et al., 2003). Hiesinger et al. (2000; 2003; 2010) outlined the units based on Clementine multispectral images, and each spectrally cohesive unit was defined as a single eruptive phase (Hiesinger et al., 2003).

Of all the large mare regions studied by Hiesinger et al. (2003), Oceanus Procellarum appears to exhibit the widest age range, as well as some of the youngest basalts on the Moon (Figure 13). It also appears that most basalt units were emplaced during the Late Imbrian Period around 3.3-3.5 Ga (Hiesinger et al., 2003).

The ages of these basalts are useful in analyzing the evolution of surface roughness. As with crater degradation, explained in the previous section, when an outcrop is exposed at the lunar surface it will degrade due to micrometeorite impact and regolith accumulation (Melosh, 1989). Likewise, surface roughness is expected to decrease as sharp edges are rounded and buried by progressively thicker regolith. Indeed, this process occurs ubiquitously across the lunar surface. For example, the regolith at

the Apollo 11 landing site in Mare Tranquillitatis (3.58 Ga) is ~3-6 m deep, while that at the Apollo 17 landing site in the Taurus-Littrow Valley (3.70 Ga) was ~10 m (Stöffler & Ryder, 2001). The evolution of surface roughness over time should therefore reflect this alteration. For this reason, a suite of mare basalts of varying ages were analyzed for their surface roughness values.

2.2. LASER ALTIMETRY: LUNAR ORBITER LASER ALTIMETER

The Lunar Orbiter Laser Altimeter (LOLA) is an instrument on the Lunar Reconnaissance Orbiter (LRO). LOLA's primary function is to measure topography, but it also allows for characterization of three other surface parameters: surface roughness, slope, and 1064 nm reflectance (Smith et al., 2010a). LOLA collects and analyzes lunar topography with high accuracy and high resolution measurements; compared to the Mars Orbital Laser Altimeter's (MOLA) vertical precision of ~1.5 m, spatial accuracy of ~100 m, and along-track spacing of ~300 m, LOLA has a vertical precision of 10 cm, accuracy of ~1 m, and along-track spacing of ~57 m (Smith et al., 2001; Smith et al., 2010a). Acquisition of this high-precision topography was motivated in part by the hope that LOLA

would assist in the selection of future lunar landing sites for robotic or human exploration (Smith et al., 2010b).

2.2.1 Configuration and Parameters

LOLA uses a beamsplitter to transmit five beams from each laser pulse arranged in an X pattern (Figure 14) (Smith et al., 2010b). The layout of the beams produces five parallel profiles of data that have a spacing of ~10-12 m, while each consecutive shot is separated by ~57 m due to the velocity of the spacecraft and the laser pulse rate (Rosenburg et al., 2011).

LOLA measures four main parameters of the lunar surface: slope, surface reflectivity, topography, and surface roughness. Slope is calculated by fitting a least-squares plane to a set of 4-10 spots over a 2-shot (~56 m) baseline (Smith et al., 2010a). Surface reflectivity is generated by measuring the ratio of returned to transmitted pulse energy, in the hope of detecting surface ice in polar regions (Smith et al., 2010b). For the purposes of this thesis, however, the two parameters of interest are topography and surface roughness. Topography is calculated by measuring the two-way time of flight (TOF) of the laser pulse, with a single-shot timing precision of 0.7 nanosec (Smith et al., 2010a) which

corresponds to a pulse range precision of ~10 cm (Rosenburg et al., 2011). Topography is then calculated by subtracting an average lunar radius value of 1737.4 km from each point, or by the subtraction of an areoid based on gravity models of the Moon. In this thesis, topographic data is manipulated to represent surface roughness on large length scales. The methods used to calculate this set of surface roughness values, referred to as RMS topographic variation, will be detailed fully in the next chapter. Finally, surface roughness is calculated by the spreading in time of backscattered pulses within the 5 m observation area of each laser beam from LOLA (Smith et al., 2010a). The surface roughness values measured in this way are referred to as pulse width.

2.2.2 Pulse Width

LOLA measures the time interval of each returned laser pulse, referred to as the pulse width. Surface roughness is calculated by the spreading in time of backscattered pulses – this value provides a root mean square (RMS) surface roughness at the scale of the laser footprint (5 m observation area, see red circles in Figure 14) (Smith et al., 2010a). The 5 m diameter of each spot allows for small length scale surface roughness

calculations. Heights varying by 30 cm will extend the backscattered pulse from that which would be received from level ground, with rougher topography causing the returned pulse to be broadened in time (Figure 15) (Smith et al., 2010b). Pulse width data are reported in terms of the measured time intervals in nanoseconds. An approximate scaling analysis[1] shows that a pulse width of 15 nanosec corresponds to a characteristic roughness of 20 cm inside the laser beam spot, and a 25 nanosec pulse width corresponds to a characteristic surface roughness of 70 cm. However, the quantification between pulse width and short length scale roughness on the Moon is currently incomplete. While a more complete analysis paralleling Neumann et al.'s (2003) study of Martian altimetry may modify these values somewhat, the basic relationship between increasing pulse width and increasing surface roughness is robust.

2.2.3 LOLA "Anomaly"

The LOLA "anomaly" is a term applied to a systematic problem in data acquisition LOLA exhibited after placement in orbit. Smith et al.

[1] According to the equation $\delta h = \frac{c}{2} * P$, where δh is the characteristic roughness, c is the speed of light, and P is the pulse width.

(2010a) determined the problem stems from the transition of LRO from warm to cold regions of the Moon – when LOLA is over the sunlit side of the Moon, all five channels receive continuous data returns from the surface at the normal full rate of 140 measurements/second. However, when the spacecraft is over the dark side of the Moon, only two of the five channels receive significant data returns. This anomaly occurs when cold temperatures trigger the thermal blanket attached to LOLA transmitter optics to contract, which pulls the transmitter beam out of alignment with the receiver. Therefore, the overall LOLA acquisition rate of valid data is between 80-90 measurements/second (Smith et al., 2010a). The effect of this LOLA anomaly on the data in this thesis is negligible, however, as analysis is limited to data where the full five shot pattern was being obtained. This will be discussed in detail in the following chapter.

2.3. RADAR: MINI-RF

Radar has repeatedly proven useful in analyzing surface features and terrains, when used to analyze geology both on Earth (see Gaddis et al., 1990) and on the Moon (see Pettengill & Thompson, 1967; Plaut et al., 2004; Campbell et al., 2008; Carter et al., 2009; Campbell et al., 2009a;

2009b). Historically, lunar radar data have originated from Earth-based measurements taken using the Arecibo and Green Bank Telescopes (Campbell et al., 2008). However, the Miniature-Radio Frequency (Mini-RF) radar spacecraft aboard LRO (Raney et al., 2010) has provided the newest spacecraft-based radar measurements of the Moon. Mini-SAR (Synthetic Aperture Radar) was a precursor spacecraft flown aboard the India's Chandrayaan-1 spacecraft (Nozette et al., 2010). The main objective of this craft was to map polar regions of the Moon at the S-band (12.6 cm) wavelength in an attempt to detect surficial or buried water ice (Spudis et al., 2009). Mini-RF has similar goals to those of Mini-SAR, although Mini-RF uses both S-band and X-band (4.2 cm) wavelengths, as well as two spatial resolution modes, 150 m and 30 m (Nozette et al., 2010).

2.3.1 Circular Polarization Ratio

When analyzing radar data, especially images, one typically uses S1, the first Stokes parameter, which represents the total backscattered power of an area (Raney et al., 2010). Likewise, the circular polarization ratio (CPR) of a signal describes the amount of diffuse scattering by surface features on the scale of the wavelength, or spectral scattering from rock

faces that are flat at the wavelength scale (Campbell et al., 2009b). In circularly polarized radar, incident beams can have one of two orientation directions, referred to as left circularly polarized (LCP) or right circularly polarized (RCP) directions. As this signal interacts with a surface, its polarity will change depending on the characteristics of the terrain it encounters.

When an incident beam reflects off a surface, it changes polarity to the opposite sense circular polarization of that which was transmitted (OC). High OC returns are generally caused by strong spectral reflections from surfaces much larger than the scale of the wavelength, and generally exhibit slopes facing the spacecraft and have low incidence angles (Figure 16, red arrows) (Campbell et al., 2009b). However, if an incident beam reflects off a second surface such as a rock edge or other sharp terrain feature on the scale of the wavelength (known as double bounce reflectance), it will change polarity twice, resulting in the same sense circular polarization as that which it was transmitted (SC) (Figure 16, blue arrows). It follows that if a signal reflects off an even number of surfaces it will also result in an OC, while an odd number of reflections will yield a

SC return, although the likelihood of receiving a signal decreases as the number of reflections increases due to diffuse scattering and absorption.

CPR is defined as the ratio of the same sense to the opposite sense of circularly polarized backscatter, relative to the transmitted sense (SC/OC)[2]. As a surface becomes more uneven, the chance a signal will exhibit double bounces reflectance increases, which then increases the CPR as well; indeed, on a perfectly (infinitely) rough surface, the amount of SC backscatter should equal the amount of OC backscatter, which will lead to a maximum CPR value of 1. Values greater than 1 have been observed in extremely rough environments (Campbell et al., 2009b), although these are generally correlated to water ice deposits (see Nozette et al., 2010).

2.3.2 Surface Penetrating Radar

One benefit of using radar is its ability to probe the subsurface. As with CPR, the degree to which the radar will react with the surface depends on the wavelength used; an incident radar beam has the ability to

[2] An alternate formula for circular polarization ratio is $\mu_c = \sigma^0_{SC}/\sigma^0_{OC}$, where σ^0 represents the dimensionless backscatter coefficient (radar cross section per unit area), from Campbell et al., 2009b.

penetrate the surface no more than ~10-20 wavelengths, depending on the composition of the material (the element titanium, which is generally present in the mineral ilmenite, has a negative correlation to probing depth) (Campbell et al., 2008). According to this relationship, S-band (12.6 cm wavelength) radar has the ability to probe the surface up to 1-2 m in typical mare regolith (with shallower depths for ilmenite-rich material) (Campbell et al., 2009b). Additionally, this wavelength is sensitive to surface and suspended rocks ~2 cm and larger in diameter. Likewise, P-band (70 cm wavelength) radar can achieve a depth about five times deeper (~5-10 m, depending on ilmenite content), and can detect rocks ~10 cm and larger (Campbell et al., 2009b).

These probing capabilities have significant ramifications, especially in the context of this thesis. Radar allows one to analyze the surfaces of certain geologic features, even if they are buried under meters of regolith. While regolith depth increases with age, a longer wavelength can analyze the actual surface roughness of various lunar features with ease. For this reason, examining radar data at a range of wavelengths can provide additional insight into the nature and cause of surface and near-surface roughness beyond what is possible using a single radar band alone.

METHODS

3.1 AREAS OF STUDY

Two remote sensing techniques, laser altimetry and radar, provided various means to calculate surface roughness. These techniques yielded four distinct data sets, each of which measured roughness on a different length scale: RMS topographic roughness, mean pulse width, S-band CPR, and P-band CPR. To ensure uniformity between these data sets, a standard box size was defined and applied to all measurements. These boxes measured 0.2 x 0.2°, or ~6 x ~6 square kilometers[3], and were centered on each feature. Multiple areas were sampled in each study region to minimize the effects of outliers.

[3] This can be checked with the relationship $\frac{2\pi R}{360^\circ}$, where R = Radius of the Moon, 1737.4 km (Smith et al., 2010). This calculation shows 1° = 30.323 km. Note: the size of a degree longitude varies slightly depending upon latitude; however, this variability does not have a large effect on the data.

3.2 ALTIMETRY DATA

The first remote sensing technique, laser altimetry, was generated by LOLA. As discussed in the previous chapter, LOLA's five spot configuration, as well as its high surface resolution, provide unique capabilities for calculating surface roughness.

3.2.1 RMS Topographic Roughness

LOLA's configuration (Figure 14) allows sequential shots to be grouped into longer profiles of the lunar surface. In order to calculate surface roughness on longer length scales, three consecutive shots, each consisting of five laser spots, were grouped together. The latitude, longitude and radius data from these spots were then used to generate a least-squares best fit plane. Effective roughness was calculated by measuring the root mean square (RMS) offset of each measured LOLA point from this idealized plane.

3.2.1.1 Generating the Least-Squares Best Fit Plane

The process of least squares is a statistical technique of fitting an ideal figure (line, plane, etc.) to a set of data by minimizing the average

squared residuals. In altimetry data, there exist three main variables – longitude, latitude, and radius – and it is therefore possible to create a three-dimensional best-fit plane to the LOLA data (Figure 17). In this instance, the residuals to be minimized lie in the Z-direction, which comprise the radius data. The calculation of the least-squares plane follows from the equation $\mathbf{Gm} = \mathbf{d}$, where $\mathbf{d}$ is the data vector, $\mathbf{m}$ is the model vector, and $\mathbf{G}$ is a m x n matrix, where m is the number of unknown parameters in the fitting model and n, when fitting a least-squares best fit plane, is 3.

This equation can be solved for $\mathbf{m}$ by multiplying each side of the equation by the transpose matrix $\mathbf{G}^T$, so that $\mathbf{G}^T\mathbf{G}\ \mathbf{m} = \mathbf{G}^T\mathbf{d}$. Multiplying both sides of this equation by the inverse matrix $[\mathbf{G}^T\mathbf{G}]^{-1}$ results in vector $\mathbf{m} = [\mathbf{G}^T\mathbf{G}]^{-1}\ \mathbf{G}^T\mathbf{d}$. This vector contains the parameters for the least-squares best fit plane. This process was used to calculate surface roughness on long (~50 m) length scales. The methods used to do this are described below.

3.2.1.2 Altmap.m, Analysis of LOLA Data

In order to determine RMS topographic roughness, MATLAB (R2011a) was used to compose a program, altmap.m, that calculated surface roughness, among other values (see Appendix A for a transcript of altmap.m). This script first read in a LOLA reduced data record (RDR) file, obtained from the Lunar Orbital Data Explorer (ODE) website[4]. Each RDR file contains data from multiple orbits of the spacecraft, so the code separates the data into individual orbits. Within each single orbit, three consecutive shots (each consisting of five spots as seen in Figure 14) were grouped together and analyzed. After these three were completely analyzed, the program preceded to the next sequential shot, and again looked at a group of three shots, and so on (Figure 18).

Once the program isolated three shots, it extracted longitude, latitude, radius, pulse width, and flag data from the RDR file. Based on the flag data[5], all invalid data points were removed. The program then subtracted each data point in the three shots from the first data point (which represents the data from a single laser beam, defined as spot 1);

[4] Lunar ODE website URL: http://ode.rsl.wustl.edu/moon/index.aspx

[5] If LOLA received data fully, the flag value is 0; if an error occurred while collecting data, the flag value for the malfunctioning spot is set to a nonzero value, generally 89, 65, etc. Errors are often generated from the LOLA "anomaly" described in Section 2.2.3.

this caused spot 1 to have a value of zero, which simplified later calculations.

These data were then used to create a least-squares best fit plane, following the method described in the previous section. To ensure robust least squares planes, a minimum of nine functioning spots was required over the three shots; if all spots received data, there were a total of fifteen points (each plane generally contained 14-15 points). This excluded data shots affected by the LOLA anomaly. After each plane was generated, the root mean square (RMS) misfit was calculated from each point to the plane according to the equation Ax + By + C = $\widetilde{D}$, where A, B and C were taken from the **m** vector calculated for the least-squares plane, and $\widetilde{D}$ is the vector of calculated ideal values. The RMS misfit was calculated on the difference between $\widetilde{D}$ and **d**. This misfit correlates to surface roughness, as a perfectly smooth surface would have a misfit of zero; analogously, the larger the misfit, the greater the surface roughness.

The mean slope of the lunar surface was then calculated in altmap.m. This measurement was performed by calculating the angle between a horizontal plane and the best-fit plane, according to the equation $\cos\theta = (|A_1A_2 + B_1B_2 + C_1C_2|) / (\sqrt{(A_1^2 + B_1^2 + C_1^2)}\sqrt{(A_2^2 +}$

$B_2^2 + C_2^2$)), with A_1, B_1 and C_1 taken from the **m** vector, and A_2, B_2 and C_2 representing a horizontal plane where $A_2 = 0$, $B_2 = 0$, and $C_2 = -1$. This calculation gives the mean slope of the surface analyzed by LOLA.

Pulse width was calculated next by averaging the pulse width values over all spots in each orbit. Finally, the program created an output matrix containing coordinates, RMS topographic roughness, mean slope, and average pulse width data. Histograms of RMS topographic roughness, mean slope, and average pulse width were also produced.

3.2.2 Pulse Width

As discussed in the previous chapter, pulse width measurements recorded by LOLA provide an additional calculation of surface roughness, albeit on a shorter length scale (~5 m) compared to RMS topographic roughness. For this reason, altmap.m calculated the mean pulse width for each study region. As previously mentioned, pulse width is a measure of roughness within each 5 m diameter illuminated spot; these values were averaged over all spots in an orbit to ensure the data were indicative of each geologic feature as a whole.

3.2.2.1 Pulse Width Slope Correction

A caveat of the pulse width measurement method is that surface slopes affect signal returns. If a surface is flat (i.e. has a slope of zero) across the 5 m observation area of the laser, the travel path of the beam remains constant (Figure 19A); however, if there is a slope across the 5 m area, one side of the beam has a shorter travel path than the other, which would broaden the beam in time (Figure 19B). This beam broadening is indistinguishable from broadening which would occur due to small-scale surface roughness.

To counteract this effect, a slope correction was applied to the altimetry data which attempts to remove the influence of slopes from the pulse width data. Slope values were measured by altmap.m, as discussed in Section 3.2.1.2. These slopes were then converted to a correcting term, which was subtracted from the original pulse width value, yielding a slope corrected pulse width value. The correction applied to the pulse width data follows from Neumann et al.'s (2003) analysis of Martian pulse width. The formula is: Original Pulse Width – $(4h^2/c)$*Tan($\frac{\pi}{180}$*Slope), where h is the laser one-way range, which for LOLA is 50 km (Smith et al.,

2010b), c is the speed of light, and Slope is the value calculated in altmap.m.

3.3. RADAR DATA

Both RMS topographic roughness and mean pulse width originated from laser altimetry data. The other two data sets used in this thesis, S-band and P-band CPR, used radar data from the Mini-RF spacecraft (Nozette et al., 2010; Raney et al., 2010), as well as Earth-based radio telescopes at Arecibo and Green Bank Observatories (Campbell et al., 2009a; Campbell et al., 2009b). Measurements of the lunar surface at two radar wavelengths, S- and P-band (12.6 and 70 cm), provided information about the roughness of the surface at different length scales, since the radar return is most sensitive to roughness on the scale of the wavelength used. These length scales are shorter than those from the altimetry data.

3.3.1 Data Collection

The observation and quantification of CPR data for the various lunar features required several steps. A shaded relief of a LOLA DEM[6] with a resolution of 128 pixels/deg provided a basemap in ArcMap 10. This basemap allowed for the identification of radar footprints for each study area. After acquiring the appropriate radar data[7], the .img and .lbl files for each footprint were used to generate .cub files, which were then loaded into ArcMap. The file conversion from .img to .cub was performed using the USGS Integrated Software for Imagers and Spectrometers (ISIS) (Torson & Becker, 1997). The data used a sinusoidal equal-area projection. In ArcMap, CPR values were gathered within the same 0.2 x 0.2° boxes as with the previous data sets. The application of both wavelengths, in addition to the measurements supplied by RMS topographic variation and pulse width, provided surface roughness calculations on a wide range of length scales. For each of the geologic features studied, average values for RMS topographic roughness, pulse width, and their associated errors, as

---

[6] The LOLA DEM is available on the Planetary Data System (PDS) website. A description of the data is available at URL: http://pds-geosciences.wustl.edu/lro/lro-l-lola-3-rdr-v1/lrolol_1xxx/data/lola_gdr/cylindrical/img/ldem_128.lbl

[7] All radar data was downloaded in the form of .img and .lbl files from the Planetary Data System (PDS) website, URL: http://pds-geosciences.wustl.edu/dataserv/moon.html

well as mean and standard deviation CPR values, are recorded in Appendix B, and will be analyzed in the following chapter.

3.4 MARE FLOWS OF VARIOUS AGES

The methods for analyzing the surface roughness of mare units of varying ages are identical to those of the other geologic features. The process for choosing specific mare units, however, was based on Hiesinger et al.'s (2010) lunar map (Figure 13). Between 6-8 units were chosen for each of three age groups: Young (1.2-1.68 Ga), Middle (2.44-2.62 Ga), and Old (3.75-3.81 Ga). When possible, two different areas were analyzed within the same unit. The areas analyzed in this project are outlined in white in Figure 13. All the units which were analyzed, as well as their ages and surface roughness data, are recorded in Appendix C.

3.5. ASSOCIATED ERRORS

The errors associated with each measurement parameter are recorded in Appendices B and C. Standard deviations were calculated in

altmap.m for both RMS topographic roughness and mean pulse width; additionally, standard deviation values for all CPR data were calculated in ArcMap. Representative error bars are placed on all plots in the following chapter. Many of the standard deviation values are quite large compared to their correlating roughness parameters. However, these values appear to be a function of actual geologic variations on the features, as opposed to measurement uncertainties. Indeed, the associated measurement uncertainties of each parameter are lower than the standard deviation values recorded in the data. Associated uncertainty of the RMS topographic variation, for example, is comparable to that of the LOLA ranging uncertainty, which is 9 cm (Smith et al., 2010a). Pulse width data, however, has not been completely calibrated, which is a contributing factor to why the data are so noisy (Gregory Neumann, personal communication, 2012). CPR data also demonstrate large standard deviation values in the data, but actual uncertainties are much less: Mini-RF data has an S-band noise equivalent of -33.6 dB at 50 km altitude (Nozette et al., 2010), while Arecibo P-band data has an uncertainty of <1 dB (Campbell et al., 2009b).

RESULTS

In this section, results from this study are summarized, and the surface roughness data for each geologic unit are provided in Appendix B. Surface roughness is compared on a range of length scales, from large-scale (~50 m) causes of roughness, such as topographic variation and large boulders, to small-scale (centimeter-decimeter) roughness features, such as regolith and small rocks on the surface and subsurface. Additionally, a suite of mare units of varying ages is evaluated to compare surface roughness on these various units as a function of age.

4.1 COMPARISON OF PULSE WIDTH AND TOPOGRAPHIC ROUGHNESS

The topographic roughness measurements attained in this study are a function of surface roughness on a scale of ~50 m, while pulse width measures the small-scale surface roughness within a 5 m diameter area. The plot of slope corrected pulse width versus topographic roughness

(Figure 20A) shows a slight positive correlation, which indicates that small-scale surface roughness correlates with roughness on a larger scale as well. This observation is consistent with the expectation that a rough, blocky surface will likewise be rough on smaller scales.

4.1.1 Volcanic Domes

The analysis of various volcanic domes, namely the Marius Hills domes, Gruithuisen and Mairan domes, and Rümker Hills complex, yielded varying results. The Marius Hills domes demonstrate similar topographic roughness values to the Gruithuisen, Mairan and Rümker Hills domes, although the Gruithuisen, Mairan and Rümker Hills exhibit higher pulse width values than the Marius Hills domes. The Rümker Hills demonstrate very low signatures in topographic roughness, but which remain in the lower range of the other dome units.

4.1.2 Mare Lava Flows

Both smooth and rough mare lava surfaces yielded similar surface roughness measurements. Average topographic roughness for the lava flows is 0.73 m, which is low compared to other units, while average pulse

width is 15 nanosec, relatively high compared to the other geologic features. The lower range pulse width values are similar to those of the Marius Hills domes, while the upper limits are closer to those of the Rümker Hills domes. However, the mare lava flows maintain relatively low values for topographic roughness – more similar to those of the Rümker Hills domes.

4.1.3 Dark Mantle Deposits

The dark mantle deposits (DMD's) exhibited similar values of topographic roughness and pulse width to those of the mare lava flows. The average topographic roughness is 0.72 m, while average pulse width is 14 nanosec. While average topographic roughness values are almost identical to those of the mare lava flows, the dark mantle deposits have a slightly higher average value of slope corrected pulse width.

4.1.4 Crater Features

Tycho and Copernicus craters are geologically distinct from the other terrains examined since they formed by impact rather than from volcanism. Likely for this reason, their resulting trends in pulse width and

topographic roughness values are dissimilar from the other features examined.

4.1.4.1 Crater Features: Ejecta Blankets

Areas analyzed on the ejecta blankets of both craters showed a large variability in topographic roughness values of ~0.91-2.0 m. This range of values was dispersed between pulse width values, ~15-19 nanosec. The ejecta blanket values followed a positive linear trend, unlike the other geologic features. The short length scale roughness of the ejecta blankets measured with pulse width was comparable to that of the rougher volcanic features such as the Gruithuisen and Mairan domes. However, roughness at longer length scales inferred from topographic roughness ranged higher than for the volcanic features, likely due to the large blocks and uneven terrain present on these fresh ejecta blankets.

4.1.4.2 Crater Features: Crater Floors

Analyses of the floors of Copernicus and Tycho craters yielded the highest topographic roughness values of any feature in this study, between 1.2-3.3 m, while pulse width values remained relatively constant,

at approximately 19-20 nanosec (with one anomalously low value at 15 nanosec). The crater floor topographic roughness and pulse width data have a relatively flat slope. The large values of topographic roughness, as well as the large range in the data, are likely due to the extreme variability in terrains present on crater floors (Figure 21). Additionally, the pulse width data remain at high values for all crater features. The pulse width seems to attain a maximum value of ~20 nanosec across the crater features. This apparent maximum pulse width value is comparable to the maximum pulse width observed on the Gruithuisen and Mairan domes.

4.1.5 Maria of Different Ages

A suite of mare units were analyzed to determine the relationship between age and surface roughness. However, there is not a definitive correlation between pulse width and topographic roughness for the suite of mare surfaces studied (Figure 20B). All three age groups appear evenly dispersed across the range of topographic roughness values recorded, ~0.53-0.89 m, as well as pulse width values, ~13-17 nanosec. However, the large size of the one-sigma error bars could suggest that the inherent geologic variation is masking any correlation between the parameters.

4.2 COMPARISON OF RADAR AND PULSE WIDTH

Large circular polarization ratio (CPR) values generally correspond to rougher topography (Campbell et al., 2009). This relationship holds on a length scale a few times the radar wavelength, which equates to ~1 m for S-band wavelength radar, and ~5-10 m for P-band. These length scales are most comparable to pulse width data, which is expected to be sensitive to roughness at less than 5 m, although analysis of the factors influencing LOLA pulse widths remains ongoing.

4.2.1 Radar at the S-Band Wavelength

The shorter of the two radar wavelengths, S-band (12.6 cm wavelength), is a measure of the surface roughness on a scale similar to the scale affecting the beam spreading measured by pulse width. It should be noted, however, that pulse width measurements are sensitive only to the upper few microns of the surface, while S-band radar can penetrate the surface up to 1-2 m in typical mare regolith (Campbell et al., 2009b). The comparison of S-band CPR and slope corrected pulse width data (Figure 22A) shows a weak positive correlation, with substantial scatter in

both parameters consistent with a range of small-scale surface roughness, potentially due to varied concentrations of small rocks on the surface or subsurface.

4.2.1.1 S-Band CPR: Volcanic Features

The volcanic domes examined here do not exhibit a correlation between S-band radar CPR and pulse width. The Marius Hills domes have very low pulse width values between 9-13 nanosec, and an equally small range in S-band CPR signatures of 0.52-0.65. The Rümker Hills domes, however, have lower S-band CPR values than the Marius Hills Domes, yet higher pulse widths. Pulse width values for the Rümker Hills, strangely, are similar to the Gruithuisen and Mairan domes and the crater features, in spite of CPR values which are lower than all of the other terrain types. The Gruithuisen and Mairan domes, by comparison, have the highest pulse width measurements, yet range in CPR values from moderate to high, 0.45-0.74, although the highest CPR value is found for the dome with the lowest pulse width.

As described above, the mare flows exhibit median pulse width values averaging ~15 nanosec, while S-band CPR values average 0.47. This

value is lower than the Gruithuisen, Mairan and Marius Hills domes, yet higher than the Rümker Hills domes.

While the range of pulse width values for the dark mantle deposits varied between ~15-19 nanosec, the S-band CPR remained mostly between 0.42-0.6, with the exception of one outlier of 0.18. A caveat to keep in mind is that the probing depth of S-band CPR is ~1-2 m, while the DMD's may in some locations only be a few centimeters thick. These CPR signatures could therefore be sensitive to material underlying the dark mantle deposits themselves. Overall, there does not appear to be a strong trend between pulse width and S-band CPR data for the volcanic features analyzed in this study.

4.2.1.2 S-Band CPR: Crater Features

Both ejecta blanket and crater floor analyses yielded similar data. Pulse width measurements for the crater features averaged ~18 nanosec, while S-band CPR values were larger than all other features (with the exception of one low outlier with a value of 0.42). The average CPR value for the crater features is 0.80. There is no definitive correlation between S-band CPR and pulse width.

4.2.1.3 S-Band CPR: Maria of Different Ages

The comparison of S-band CPR and pulse width for mare of varying ages (Figure 22B) shows a slight negative correlation. The young mare units exhibit the lowest CPR value as well as the lowest pulse width value (0.37 and ~13 nanosec, respectively), while the old mare units contained the highest CPR (albeit at a low pulse width. 0.68 and 13 nanosec, respectively). However, there is no definite correlation between the two variables that is dependent on age.

4.2.2 Radar at the P-Band Wavelength

P-band radar (70 cm wavelength) has a much longer wavelength than S-band radar, and is therefore sensitive to larger surface and subsurface rocks. While its length scale is less similar to pulse width data than S-band radar, the factors controlling both measurement parameters may still be related. Therefore, it is sensible to compare P-band CPR and pulse width data (Figure 23A).

4.2.2.1 P-Band CPR: Volcanic Features

The Marius Hills domes contain a wide variation in P-band CPR values, as well as the highest value of CPR of any volcanic feature. By comparison, the Rümker Hills domes exhibit fairly low CPR values, similar to what is observed in the dark mantle deposits and mare lava flows. Additionally, the Gruithuisen and Mairan domes exhibit moderate CPR values, but at a large range of pulse width values. While the Marius Hills domes and the Gruithuisen and Mairan domes span similar CPR ranges, their different pulse width signatures could suggest they are morphologically distinct.

The mare units analyzed showed moderate pulse width values. However, CPR values are higher in the mare units than the dark mantle deposits (with the exception of two extremely low mare CPR values), and extend into the range of the volcanic domes, ~0.35.

The dark mantle deposits, while yielding mid-range pulse width values, contain the lowest values of P-band CPR as a unit. Interestingly, the average P-band CPR value for the DMD's is 0.21, which is much lower than S-band CPR, which is 0.46. As with S-band radar, the P-band

wavelength likely penetrates the surface to depths greater than that of the pyroclastic deposits. This would result in CPR signatures of the lunar material underlying the dark mantle deposits, as opposed to the pyroclastic material itself. The low radar signatures are therefore unexpected; one would expect the buried material to be rougher on the scale of the radar compared to the pyroclastic ash mantling the surface. Overall, there does not appear to be a correlation between P-band CPR and pulse width for the volcanic features measured here.

4.2.2.2 P-Band CPR: Crater Features

The comparison of P-band CPR and slope corrected pulse width for crater features shows a trend distinct from that of the other geologic features. The range of CPR values for the crater features is extremely wide, between 0.39-1.5, while pulse width values remain relatively high throughout. There seems to be no strong distinction between the ejecta blanket and crater floor in the comparison of P-band CPR and pulse width.

4.2.2.3 P-Band CPR: Maria of Different Ages

There again appears to be no strong correlation between P-band CPR and slope corrected pulse width for maria of different ages (Figure 23B). The middle-aged and young maria have a wide variation in values for both P-band CPR and pulse width. The old mare units concentrate mostly in the upper range of pulse widths; however, they also exhibit the lowest values of P-band CPR. As with S-band CPR, P-band CPR does not correlate to pulse width when plotted as a function of age.

4.3. COMPARISON OF RADAR AND TOPOGRAPHIC ROUGHNESS

Because of the precision of the LOLA measurements, topographic roughness from point-to-point data is a quantitatively robust analysis of surface roughness at length scales of ~50 m. It is therefore valuable to compare this topographic roughness to the radar CPR measurements.

4.3.1 Radar at S-Band Wavelength

The comparison of S-band CPR and topographic roughness (Figure 24A) shows a positive correlation. This trend exists despite the difference in length scales that are expected to influence these two parameters.

4.3.1.1 S-Band CPR: Volcanic Features

In the comparison of S-band CPR to topographic roughness, the volcanic domes are not distinguishable from one another. The Marius Hills domes plot close to the CPR values of the Gruithuisen and Mairan domes, although the latter domes span a wider range of CPR values. Likewise, both sets of domes range approximately the same values of topographic roughness. Conversely, the Rümker Hills demonstrate the lowest values of both CPR and pulse width of any feature (with the exception of one anomalously low dark mantle deposit CPR value). However, these roughness values still coincide with those of the smoother geologic features, namely the mare lava flows and the dark mantle deposits.

The mare units, while exhibiting low values of topographic roughness, ranged widely in CPR values, at times exhibiting higher values than the volcanic domes. These values suggest the mare is extremely variable in surface roughness at length scales that affect S-band radar.

Similar to the mare lava flows, the dark mantle deposits vary widely in CPR values. Topographic roughness values for the DMD's

remain low despite this variability. With the exception of one extremely low value of CPR, other dark mantle deposit values of CPR are moderate as compared to the other geologic features.

4.3.1.2 S-Band CPR: Crater Features

The comparison of these parameters for the crater features shows the continuation of the positive trend of the other geologic features, although a much wider variation occurs within the crater units.

Analyses of both the ejecta blanket and crater floor regions yielded the largest roughness signatures in both parameters. Ejecta blanket data were generally lower than crater floor values, ranging from 0.42-0.82 in CPR, and 0.91-1.9 m in topographic roughness. Crater floor values continue to increase in both S-band CPR and topographic roughness. However, the maximum CPR appears to remain ~1.0, despite increasing values of topographic roughness. This feature varies in both CPR and topographic roughness, due to the chaotic terrain present in large crater floors such as Tycho and Copernicus craters. The maximum CPR values

attained by the crater floors are greater than 1, which indicate the presence of highly rough terrain[8].

4.3.1.3 S-Band CPR: Maria of Different Ages

S-band CPR values for maria of different ages (Figure 24B) remained relatively constant ~0.47, despite topographic roughness values ranging from ~0.53-0.89 m. All three age categories spanned these ranges, suggesting no correlation between the two measurement parameters that is dependent on age. However, the extremely large variation in RMS topographic roughness standard deviation could dampen an apparent correlation in the data.

4.3.2 Radar at P-Band Wavelength

Despite the dissimilarities in length scales of S-band CPR and topographic roughness, a positive trend was apparent nonetheless. The comparison of P-band CPR and topographic roughness, therefore, should yield a similar correlation, as these length scales are more comparable.

[8] Note: CPR values higher than 1 can also indicate the presence of ice, although this is not likely in the craters analyzed here.

Indeed, when P-band CPR is plotted against topographic roughness (Figure 25A), a strong positive correlation is visible, and a linear trend line yields an R^2 value of 0.81.

4.3.2.1 P-Band CPR: Volcanic Domes

Similar to the plot of S-band CPR compared to topographic roughness (Figure 24A), in the comparison of geologic features at P-band CPR and topographic roughness (Figure 25A), the volcanic domes are indistinguishable from one another. The Marius Hills domes yield the highest values at both parameters, but the Gruithuisen and Mairan domes lie along the same trend line at slightly lower values. The Rümker Hills domes follow this linear trend at yet lower values of both CPR and topographic roughness, and are indistinguishable from the mare and dark mantle deposit units.

4.3.2.2 P-Band CPR: Mare Lava Flows

The mare lava flows demonstrate relatively low values of both CPR and topographic roughness. The CPR values in the P-band wavelength, however, are lower than in S-band, although the highest values of CPR for

the mare lava units extend into the lower values for the Marius Hills, Gruithuisen and Mairan domes. The same relationship occurs with respect to topographic roughness.

4.3.2.3 P-Band CPR: Dark Mantle Deposits

In P-band CPR, unlike S-band CPR, the dark mantle deposits average lower than the mare lava flows. They are roughly equal in topographic roughness, although the DMD's are on average slightly less rough. Despite this overlap, the dark mantle deposits generally exhibit the lowest P-band radar values of any feature class.

4.3.2.4 P-Band CPR: Crater Features

The crater features extend the linear trend line when compared with the other geologic features. Both ejecta blanket and crater floor features vary widely in CPR and topographic roughness. This trend is apparent in other comparisons as well, although CPR values at the P-band wavelength are higher than at S-band. Additionally, CPR values appear to reach a maximum value of ~1.5, while topographic roughness values continue to increase.

4.3.2.5 P-Band CPR: Maria of Different Ages

Despite the strong correlation of data between features at P-band CPR and topographic roughness, the comparison of these parameters for mare units of varying ages (Figure 25B) reveals no such relationship. There is a slight increase in CPR values as topographic roughness increases, consistent with the general relationship between these two parameters. However, this trend is more likely a result of geologic variation on the different mare units rather than a signature of a significant relationship due to age, in part because of the large variation in the topographic roughness data.

4.4 COMPARISON OF RADAR SIGNATURES AT DIFFERENT WAVELENGTHS

The final comparison of parameters for the features analyzed involves comparing radar at both S- and P-band wavelengths (Figure 26A). A positive correlation between these parameters is again visible, although the correlation is not as strong as the relationship between P-band CPR and topographic roughness (Figure 25A). Average values of CPR are

different between S- and P-band wavelengths – generally S-band CPR values are higher than P-band. The exception to this is the crater features, which have larger P-band CPR signatures than are observed in S-band. Despite the higher values of CPR at the S-band wavelength, there is more variation within a given unit at the P-band wavelength. This is apparent in the Marius Hills domes, which demonstrate a particularly large variation in P-band CPR. This large variation is not seen in the other roughness parameters.

4.4.1 Maria of Different Ages

The comparison of radar at two wavelengths for maria of different ages (Figure 26B) did not yield the same trends as in the comparison of more diverse geologic units. This lack of a clear correlation has been seen throughout the previous analyses relating to age.

4.5. COMPARISON OF PARAMETERS TO AGE

While the maria units of different ages have already been analyzed with respect to topographic roughness, pulse width, S-band CPR, and P-band CPR, it is also useful to compare these parameters against age

(Figures 27A-D). These parameters, however, do not show a strong dependence on age. Topographic roughness (Figure 27A), pulse width (Figure 27B), and S-band CPR (Figure 27C) do not vary significantly, while P-band CPR (Figure 27D) appears to decrease with age. These relationships are not significant enough to suggest a relationship between surface roughness and age, as measured in this study.

DISCUSSION

5.1 EFFICACY OF PARAMETER COMPARISONS

Trends are apparent when four types of observations (RMS topographic roughness, average pulse width, S-band CPR and P-band CPR) are plotted against each other. The strength of these trends varies depending on the parameters being compared. It is likely that the strength of this correlation is dependent on the relative length scale of both parameters. The expectation is that more similar length scales should have stronger correlations; however, other factors such as signal-to-noise, sensitivity of radar to the near subsurface, regolith properties, and geochemical composition may influence the results, as discussed below.

5.1.1 Radar Data Compared to Pulse Width Data

Of the four parameters, P-band CPR and pulse width are sensitive to surface properties on the most similar length scales (~5-10 m for P-band

CPR; under 5 m for pulse width). Additionally, S-band CPR and pulse width have the next closest length scales (S-band CPR length scales are ~1-2 m). Contrary to expectations, however, the correlation of pulse width with CPR at both radar wavelengths is not as strong as between other parameters measured in this study (see Figures 22A and 23A). A likely cause of the scatter in the data is uncertainty and low signal-to-noise of the pulse width measurements. As was previously noted, the pulse width data returned from LOLA have not been fully calibrated (Neumann et al., 2009) and therefore contain more noise than the other measurement parameters.

5.1.2 Radar Data Compared to Topographic Roughness

The strongest correlation seen in the data is between P-band CPR and RMS topographic roughness. This is likely due to the relative similarity in length scale between both parameters, with RMS topographic roughness sensitive to topography at a length scale of ~50 m, compared to the ~5-10 m baseline of P-band CPR data. While the similarity in length scale between these two parameters is not as close as pulse width data is to radar length scales, both RMS topographic roughness and P-band CPR

have the two longest length scales, which are relatively similar. Both parameters also have better accuracy than pulse width measurements. For these reasons, the strong correlation that is observed in the data is expected (Figure 25A).

The strong relationship between different measurements of roughness as measured by P-band CPR and RMS topographic roughness has geologic implications. Specifically, this suggests a relationship between the presence of surface and subsurface meter-sized boulders measured by the P-band radar, and larger scale topographic variation measured in the altimetry data.

The correlation of S-band CPR and RMS topographic roughness is weaker than that of P-band CPR, however. This weaker signature is likely due to a shorter (12.6 cm) wavelength and hence sensitivity to roughness on shorter length scales as compared to P-band. This difference between S-band signatures and RMS topographic roughness measurements leads to a weaker correlation in the data. In geologic terms, there is a relationship between the decimeter-meter sized rocks being measured by S-band CPR and the larger scale topographic roughness; however, this

relationship is not as strong as the apparent relationship between larger rocks and the variation in topography.

5.1.3 Pulse Width Compared to Topographic Roughness

The pulse width measurements and RMS topographic roughness should be sensitive to similar scales of surface roughness. However, as seen in Figure 20A, there is not a strong positive trend in the data. This is interpreted to be due to the large uncertainties in the pulse width data.

5.1.4 Radar Comparisons at Different Wavelengths

P-band versus S-band CPR (Figure 26A) is expected to have a fairly strong correlation, since the length scales of both wavelengths are relatively comparable. The difference in the length scale which these two radar bands are sensitive is much less than the difference between S-band wavelength and RMS topographic roughness, for example. There is a correlation visible when comparing both radar parameters, although it is not as strong as the comparison of P-band CPR and topographic roughness. This is likely due to the fact that the two wavelengths measure surface and subsurface rocks on different scales; the presence of large,

meter-scale rocks does not necessitate a higher concentration of decimeter-scale rocks. While boulder-sized rocks detectable by P-band CPR generally originate from crater ejecta (Bart & Melosh, 2010), S-band CPR is sensitive to much smaller particles and rocks which are more ubiquitous in lunar regolith (Langevin & Arnold, 1977). Large boulders will eventually erode into smaller cobbles and pebbles due to micrometeorite bombardment, but this process occurs continuously across the entire lunar surface. Therefore the rate of regolith evolution that would lead to enhanced S-band CPR signatures occurs on different time scales than those that would enhance P-band CPR.

5.2 GEOLOGIC INTERPRETATIONS

By analyzing the data trends of various lunar features, it is possible to draw certain conclusions about their geology. Certain trends were expected; for example, the dark mantle deposits and mare units were smooth on most roughness scales, while crater features were rough on all scales. Additionally, other geologic conclusions can be drawn from the data. The Marius Hills and the Gruithuisen and Mairan domes are thought to have differing composition (Sunshine et al., 1994; Weitz &

Head, 1999; Wilson & Head, 2003; Campbell et al., 2009b; Besse et al., 2011). It was therefore expected that there would be a distinction in roughness measurements on various length scales between both compositional groups; silicic domes are generally regarded as extremely rough, and have been observed to exhibit high values of radar backscatter (CPR ~0.3-0.95) (Plaut et al., 2004). However there is no significant distinction in surface roughness values in the Marius Hills or the Gruithuisen and Mairan domes across multiple data sets. This may suggest that the roughness signatures exhibited by volcanic domes as measured in this thesis are not strongly dependent on composition.

Alternatively, the Rümker Hills appear distinct from the other dome features in most data sets. Indeed, the Rümker Hills are indistinguishable in roughness data from the mare lava flows and dark mantle deposits. This supports the theory that the Rümker Hills may be mantled by multiple meters of fine-grained pyroclastic material (Weitz & Head, 1999; Campbell et al., 2009b).

An unexpected result was a large spread in P-band CPR values for the Marius Hills domes (0.24-0.91, Appendix B). Campbell et al. (2009b) found a relatively large spread in P-band values for these domes (0.48-0.91)

as well, although the lower limit measured in this thesis is much lower, and is similar to values measured in the surrounding mare plains. This large variation in CPR values could be caused by morphological differences between specific domes; the area and height of domes vary, leading some domes to have steeper sides than others. Weitz and Head (1999) suggest that domes with steeper sides formed during extremely late stages of eruption and very low mass fluxes, while earlier flows would have formed the flatter domes.

When comparing different roughness parameters, data originating from crater features often follow different trend lines compared to those followed by the other volcanic features (i.e. S-band CPR versus topographic roughness, Figure 24A). This distinction is expected – the emplacement mechanisms by which the volcanic features are created vary depending on the unit, but all originate due to igneous processes. The crater features, however, are impact-generated. It is therefore unsurprising that they demonstrate distinct surface roughness signatures.

5.3. EFFECTS OF REGOLITH DEVELOPMENT ON SURFACE ROUGHNESS

There appears to be no correlation between the age of the various units and their surface roughness. This lack of a correlation may result from two key factors: first, the regolith accumulated in ~1 Ga (since the emplacement of the youngest mare unit, 1.2 Ga) is significant enough to homogenize the roughness signatures of a flow on the scales analyzed in this thesis (namely decimeter-meters measured by S- and P-band CPR; ~5 m measured by pulse width; and ~50 m measured by RMS topographic roughness). Second, further regolith accumulation after ~1 Ga does not lead to significant evolution in the overall surface roughness measured by these methods.

If we assume a regolith accumulation rate of ~2 m/Ga (Langevin & Arnold, 1977), it is expected that S-band CPR data would not have a sufficient probing depth to measure the unfragmented portion of a young (~1 Ga) mare flow. Likewise, data gathered from LOLA is only sensitive to the uppermost microns of the surface (Smith et al., 2010b). However, the wavelength of P-band CPR would be expected to penetrate to a depth that could measure the surface of relatively young mare flows through the

regolith that has accumulated over ~1 Ga. Despite this, there does not appear to be a large variation in young mare CPR data at P-band wavelengths as compared to other parameters. This could also suggest the paucity of surface or subsurface boulders on the scale of the P-band radar for the maria units analyzed.

One final caveat associated with these measurements is that radar signatures are dependent on the composition of which they are analyzing. Specifically, titanium (usually in the mineral ilmenite, $FeTiO_3$) can lead to increasing attenuation of radar signals as concentration increases (Campbell et al., 2009b). Therefore probing depths would be dampened in a regolith with high ilmenite content. This factor could complicate the interpretation of radar signatures on maria with different compositions.

CONCLUSION

Through the application of two different remote sensing techniques, it is possible to calculate and compare the surface roughness of various lunar features. The technique used in this study represents a unique method of quantifying roughness, whereby data sets from LOLA altimetry and Earth- and satellite-based radar are applied to measure and then compare surface roughness on distinct length scales. This comparison of RMS topographic roughness, pulse width, P-band and S-band CPR allowed for the analysis of various sources of surface roughness. The study of not only lunar volcanic domes, but also various other lunar features, including mare flows, dark mantle deposits, and young craters provided a range of geologic unit types to sample in this thesis.

Through the comparison of these parameters, several relationships became apparent. A positive-trending relationship is present when comparing all roughness parameters, the strongest of which is between P-

band CPR and RMS topographic roughness values. Additionally, the Marius Hills appear indistinguishable from the Gruithuisen and Mairan domes in much of the roughness data. Conversely, the Rümker Hills data appear distinct from the other dome units in most data sets, and appear to have roughness signatures more similar to that of the mare and dark mantle deposit units. The Marius Hills domes vary widely in P-band CPR values, which is likely due to variation in morphological characteristics between domes. Additionally, crater features generally follow different trend lines in the data compared to the volcanic units; this is due to the dichotomy in emplacement mechanisms of the two types of features.

An additional analysis was performed to ascertain the affects of regolith development on surface roughness of maria. There was not an apparent correlation between roughness and age for mare units of varying ages, suggesting the regolith accumulated after the first ~1 Ga post-emplacement is sufficient to homogenize roughness signatures such that they are indistinguishable from maria of greater ages, and that further regolith accumulation does not affect these signatures greatly.

6.1 AREAS OF FUTURE STUDY

While the research described here represents a comprehensive analysis using the methods described, there are several additional components which would complement the present results. Weitz and Head (1999) propose that morphology of the Marius Hills domes may depend on the stage of eruption; testing and verifying this theory would provide an interesting addition to the data collected thus far.

The addition of X-band (4.2 cm) CPR data from the Mini-RF spacecraft (Nozette et al., 2010) would also provide an additional measure of surface roughness on shorter length scales. This additional parameter would be of particular interest when analyzing the Rümker Hills and dark mantle deposits, as well as mare units of varying ages, as they appear to be dominated by smaller surface and subsurface rocks. Additionally, comparison of ground-based S-band CPR values from Arecibo (Campbell et al., 2009b) to spacecraft-based S-band CPR values from Mini-RF may help clarify systematic differences in ground-and-spacecraft based observations, which may have implications for this study.

As discussed in the previous chapter, radar penetration depth is dependent on composition, particularly the abundance of titanium (Figure

28). For this reason, when analyzing mare units of different ages, it is useful to understand the variation of titanium content across mare units as well. Data on elemental titanium abundances have been measured on the Moon with the Gamma Ray Spectrometer on the Lunar Prospector spacecraft (Prettyman et al., 2006). An initial comparison of composition and radar properties suggests that the relationship may be complex, however, and analysis is ongoing.

As data is continuously gathered by LRO, it will become possible to create a global surface roughness map at various length scales (e.g., Figure 29). These maps would allow for roughness values to be compared across the entirety of the lunar surface (with the exception of P-band data, as ground-based radar cannot reach the lunar farside). The creation of these maps could uncover new surface roughness properties of different geologic units on the Moon, revealing fundamental characteristics about the lunar surface.

FIGURES

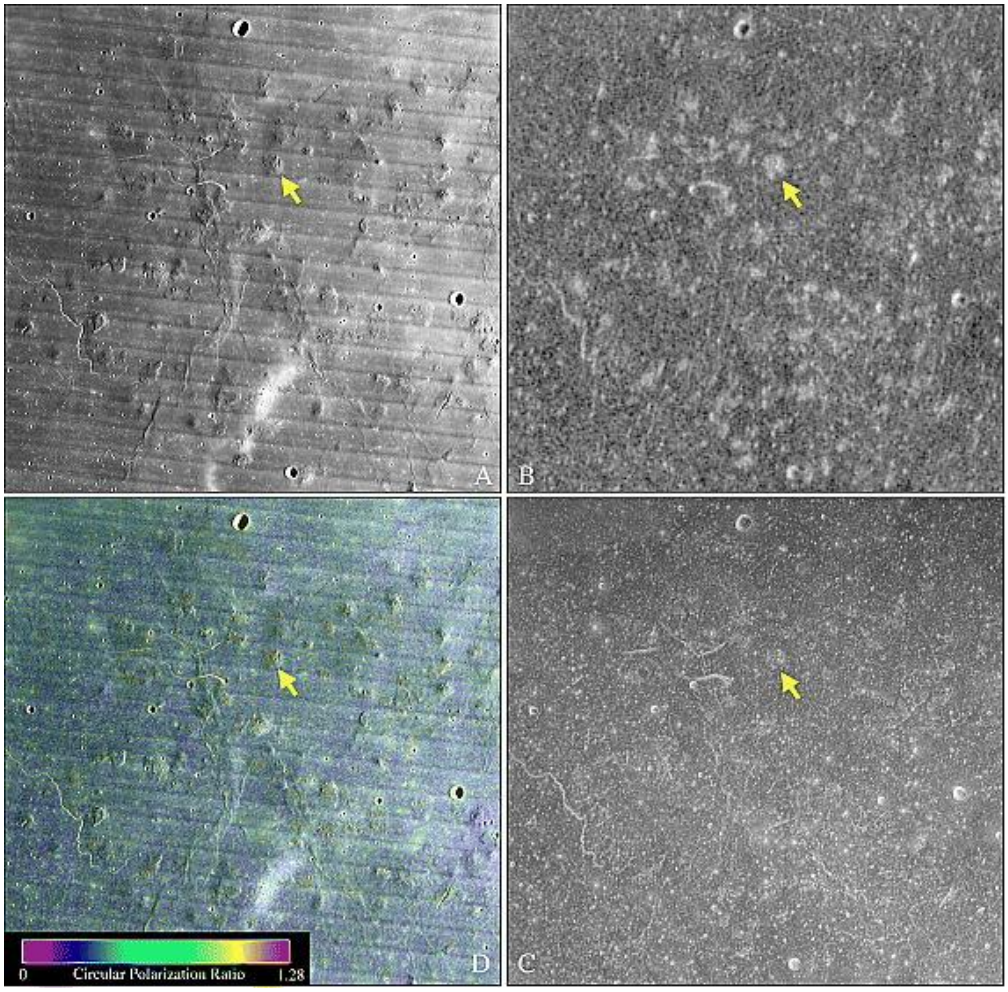

Figure 1. Marius Hills Domes. (A) Lunar Orbiter photo IV-157/H2; (B) P-band (70 cm) same-sense circular polarization backscatter image; (C) S-band (12.6 cm) same-sense circular polarization backscatter image; (D) S-band circular polarization ratio color overlay on Lunar Orbiter IV photo. The domes are of a noticeably higher CPR than the surrounding mare. From Campbell et al., 2009b.

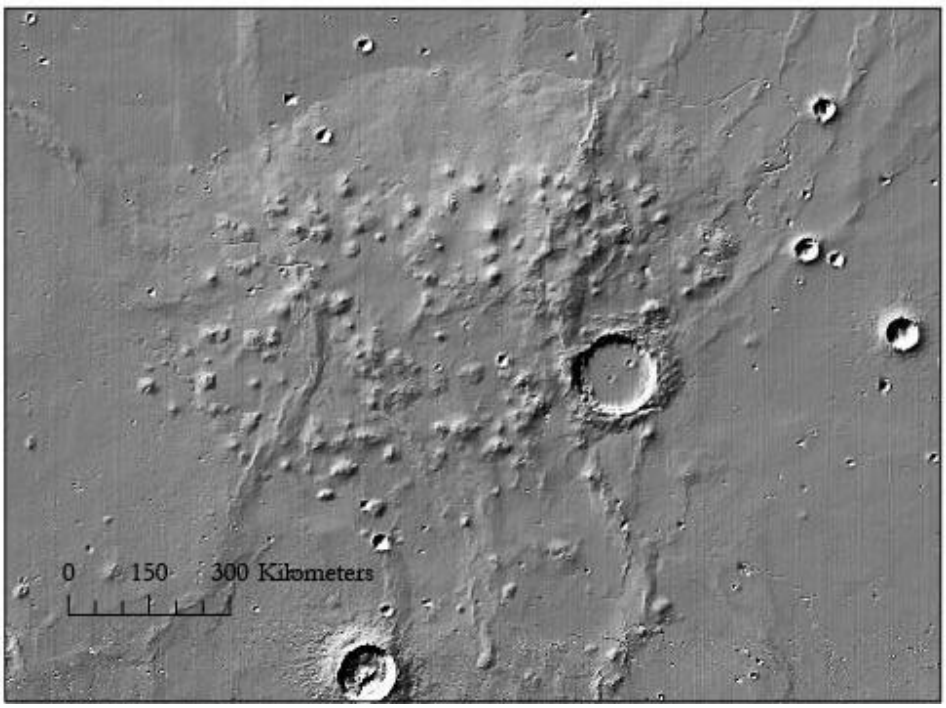

Figure 2. LOLA Shaded relief map of the Marius Hills Complex in Oceanus Procellarum.

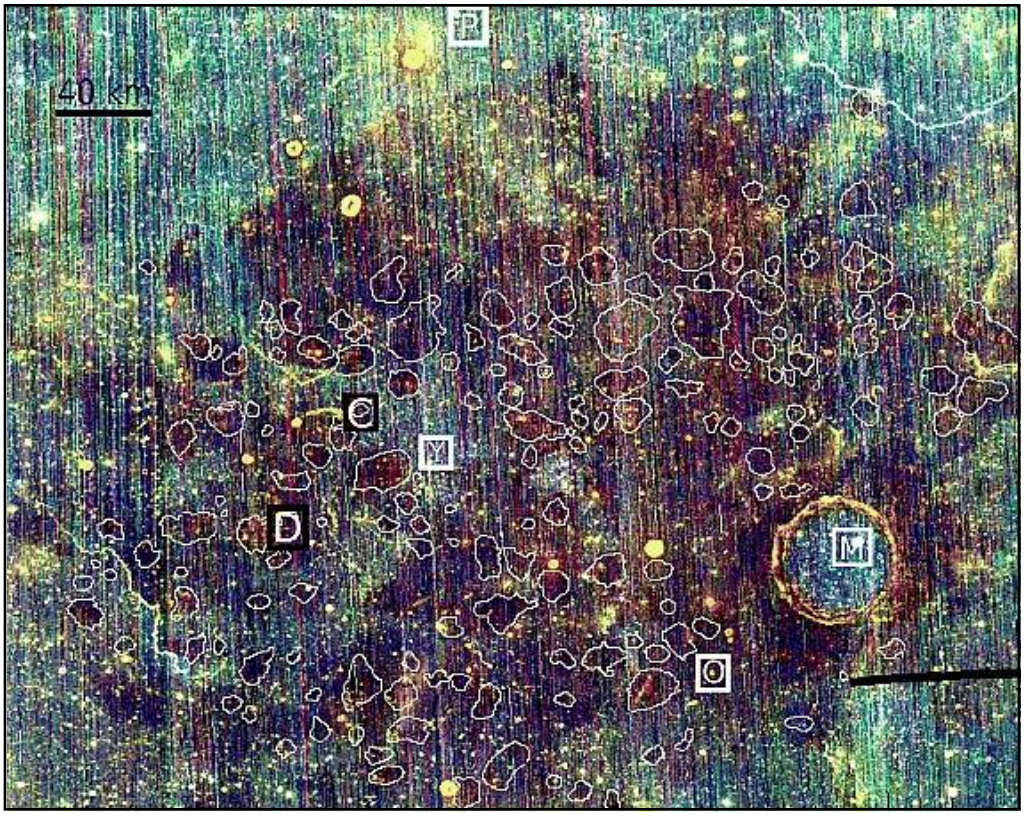

Figure 3. Color composite spectral image of the Marius Hills Complex using M^3 data. Red, green, and blue colors correspond to reflectances at three wavelengths: red at 950 nm, green at 1050 nm, and blue at 1250 nm. White lines indicate boundaries of volcanic domes. Bluer regions indicate olivine-rich regions, with a stronger 1250 nm absorption, while red-purple regions indicate pyroxene-rich regions due to stronger 950 nm absorption. From Besse et al., 2011.

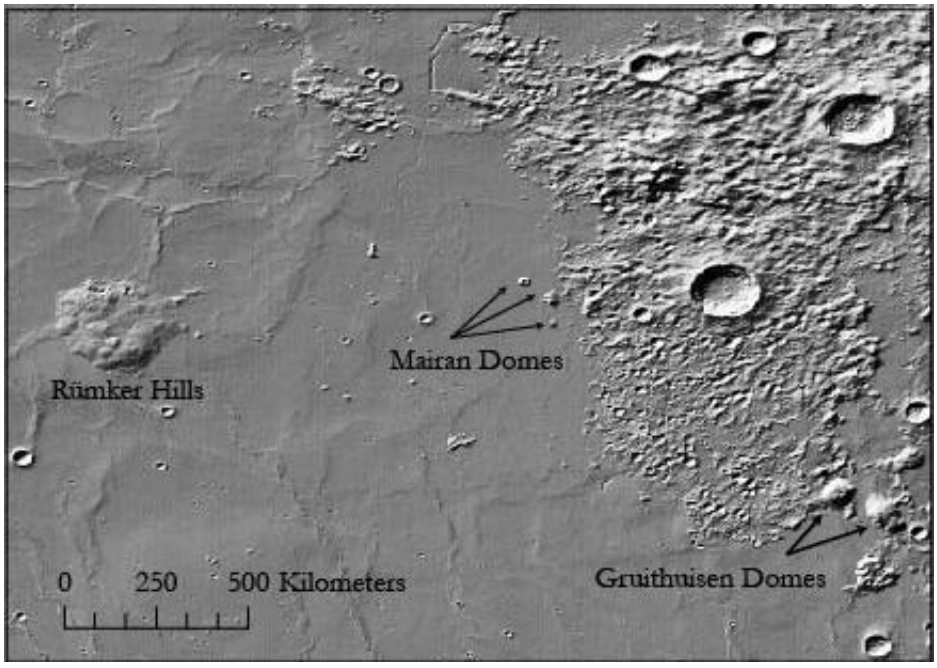

Figure 4. LOLA Shaded relief map of the Rümker Hills, Gruithuisen Domes and Mairan Domes in northern Oceanus Procellarum.

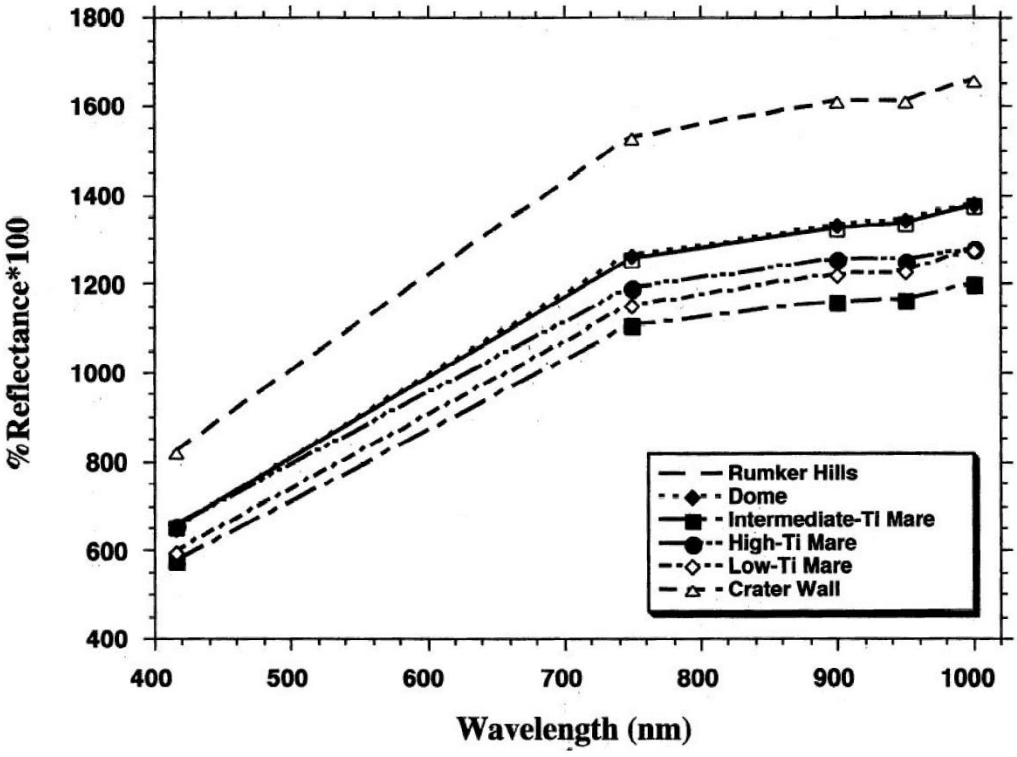

Figure 5. Spectra of the Rümker Hills Complex and surrounding mare using Clementine spectra. The domes (filled diamonds) are spectrally identical to the mare on Rümker Hills (solid line). The large values for the crater wall unit (open triangles) represent secondary craters in the north that could indicate the presence of buried highland material which was excavated post-impact. From Weitz & Head, 1999.

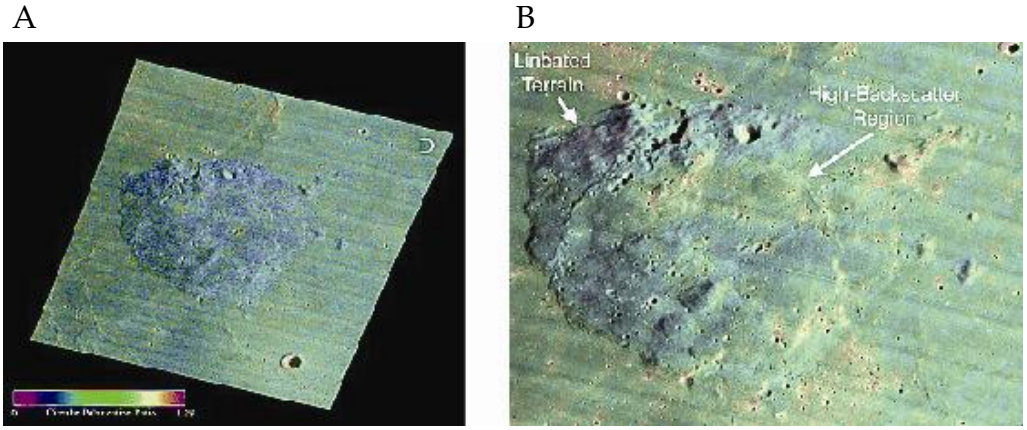

Figure 6. Circular polarization ratio (CPR) images of the Rümker Hills. CPR values are shown as a color overlay on Lunar Orbiter IV-163/H2. (A) S-band (12.6 cm) CPR; (B) P-band (70 cm) CPR. From Campbell et al., 2009b.

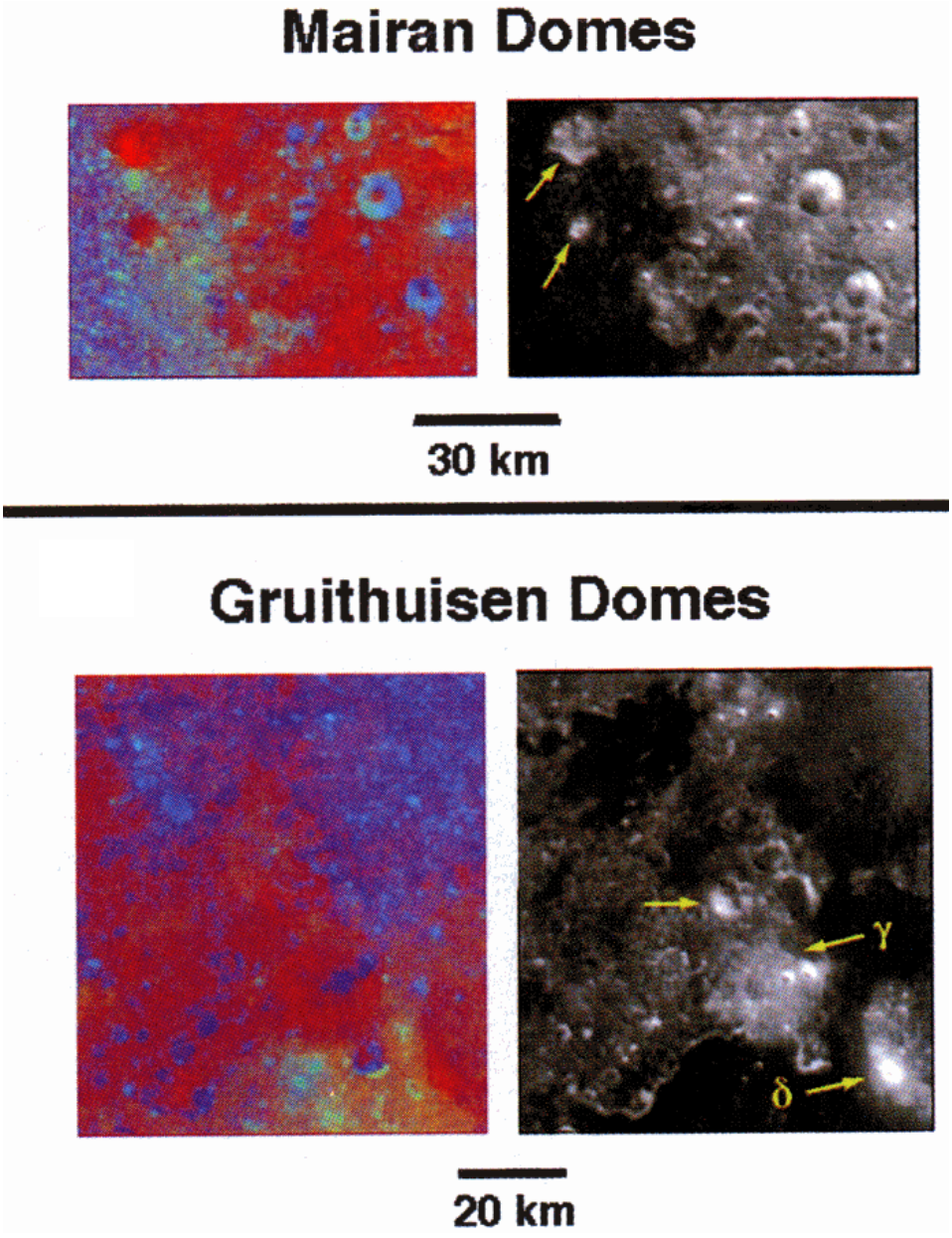

Figure 7. Color ratio images and 750 nm frames of the Gruithuisen and Mairan domes using Clementine multispectral data. The color ratios are as follows: red 750/415; green 750/950; blue 415/750. From Weitz & Head, 1999.

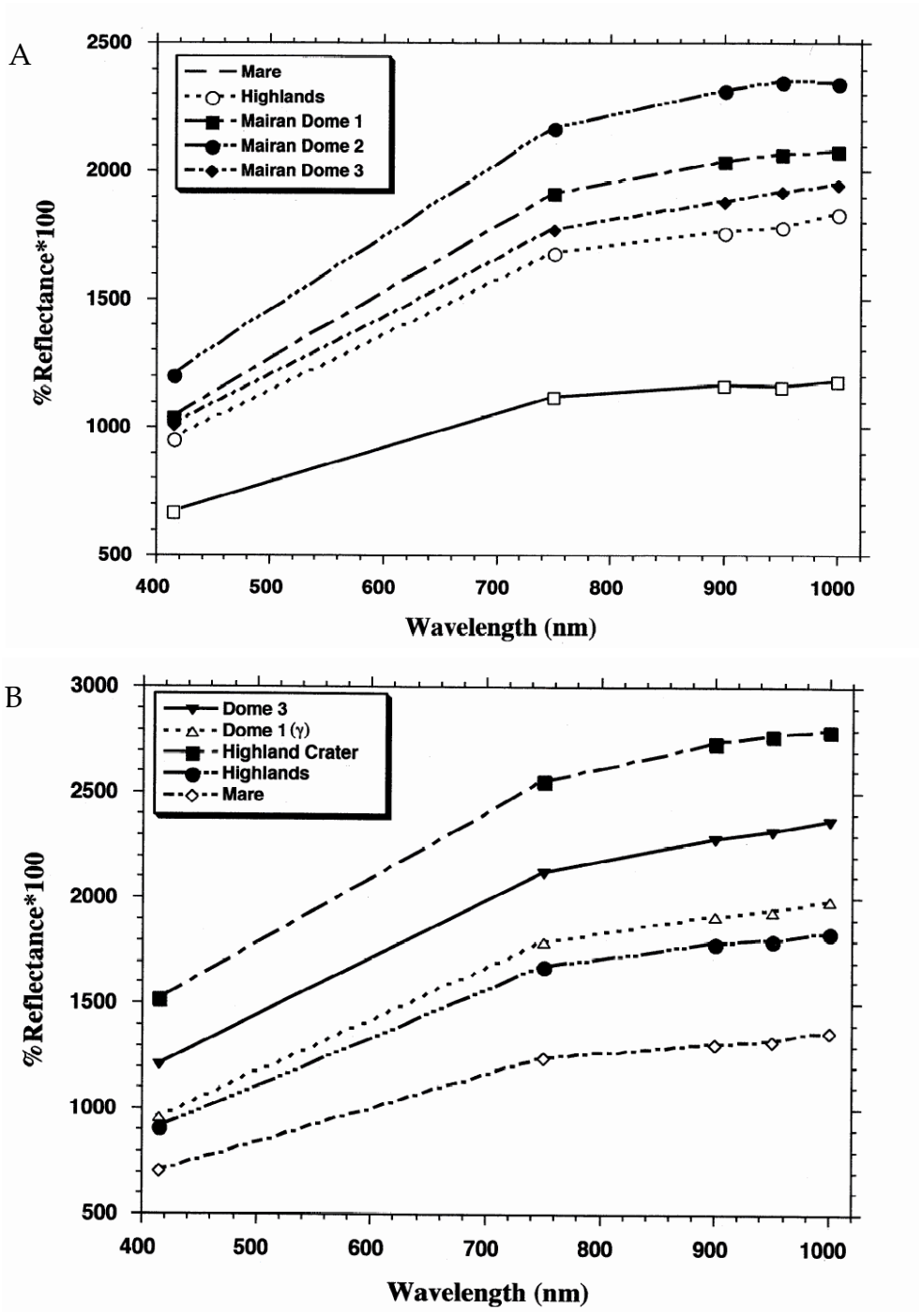

Figure 8. Spectra of (A) Mairan domes and (B) Gruithuisen domes using Clementine multispectral data. Both have characteristics of feldspathic material. From Weitz & Head, 1999.

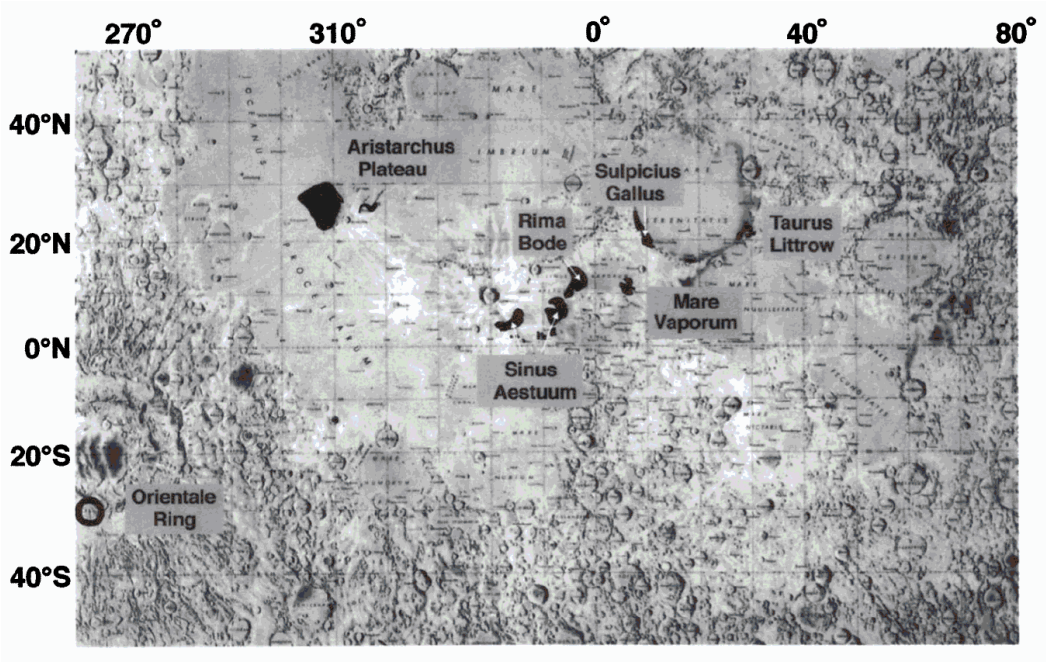

Figure 9. Locations of regional dark mantle deposits. From Weitz & Head, 1999.

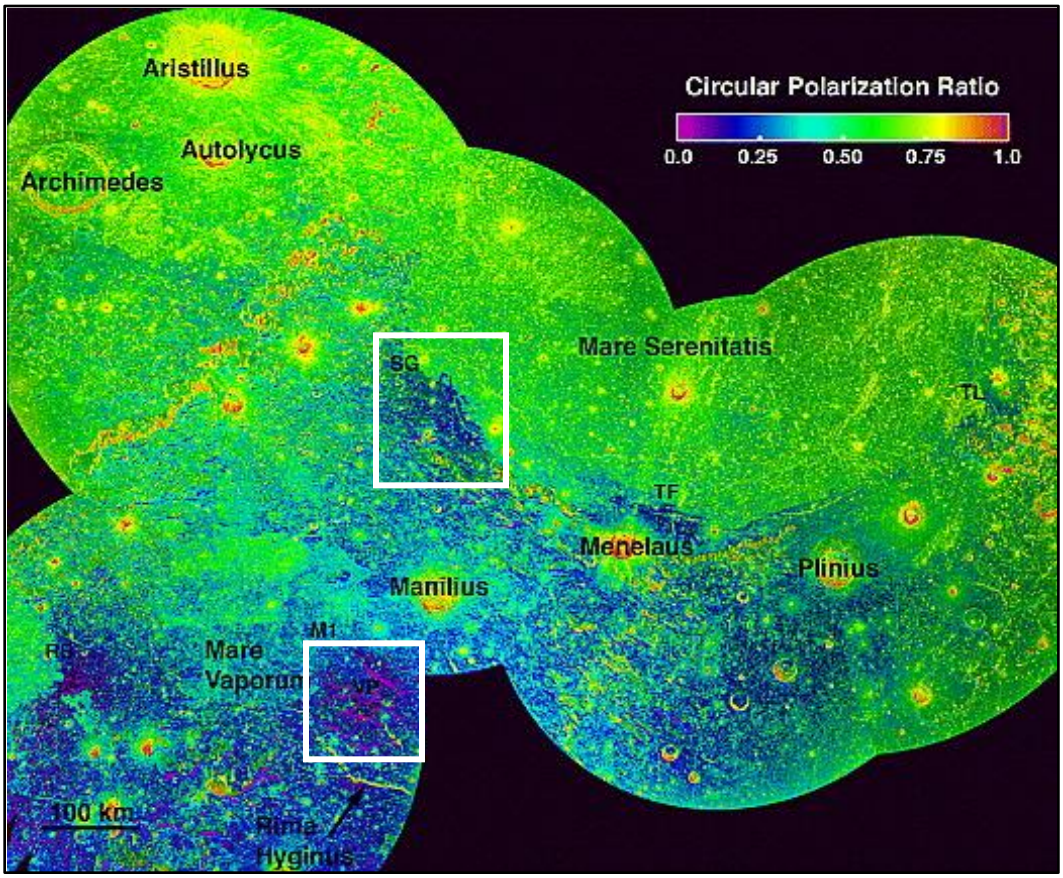

Figure 10. S-band (12.6 cm) circular polarization ratio map, with CPR color scale overlaid on OC image. Pyroclastic deposits are identifiable by low CPR values with blue and purple colors. Regions analyzed for this project in Mare Vaporum and Sulpicius Gallus are boxed. Sinus Aestuum is not visible, although also analyzed. Image from Carter et al., 2009.

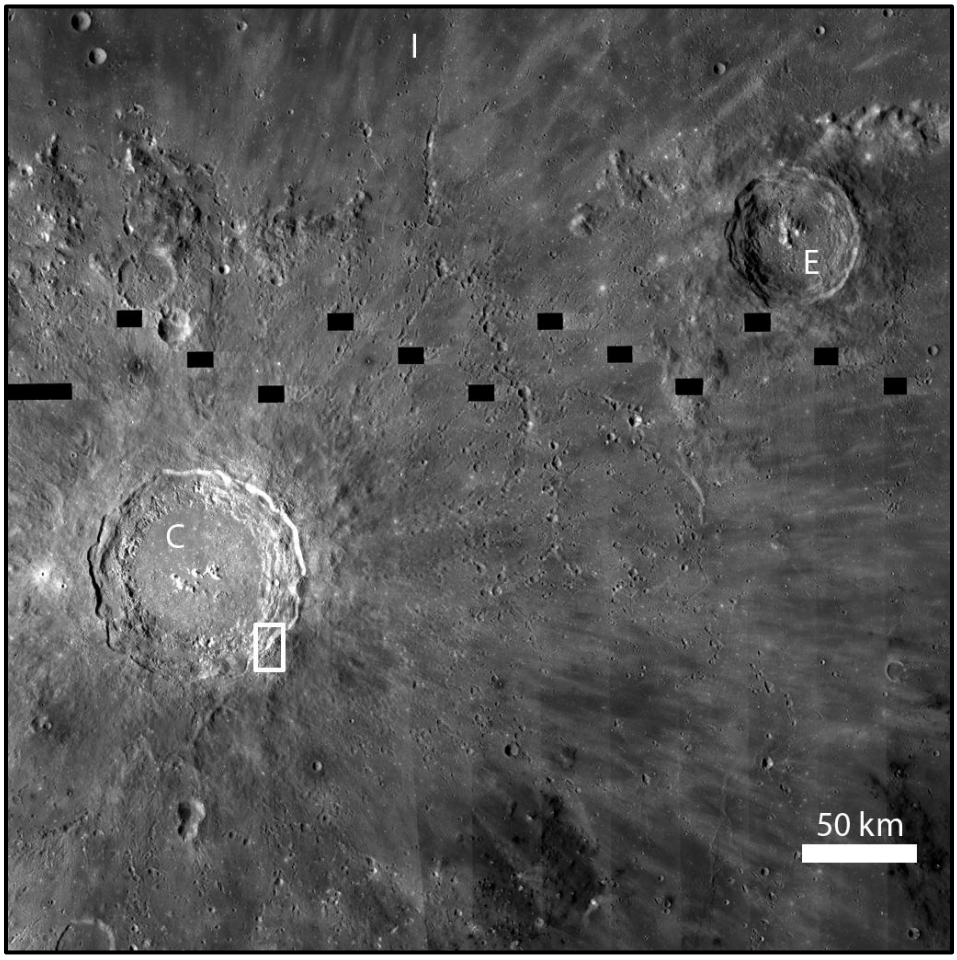

Figure 11. LROC WAC context mosaic of Copernicus crater (C), and nearby Eratosthenes crater (E), as well as the rim of Imbrium Basin (I) to the north [NASA/GSFC/Arizona State University].

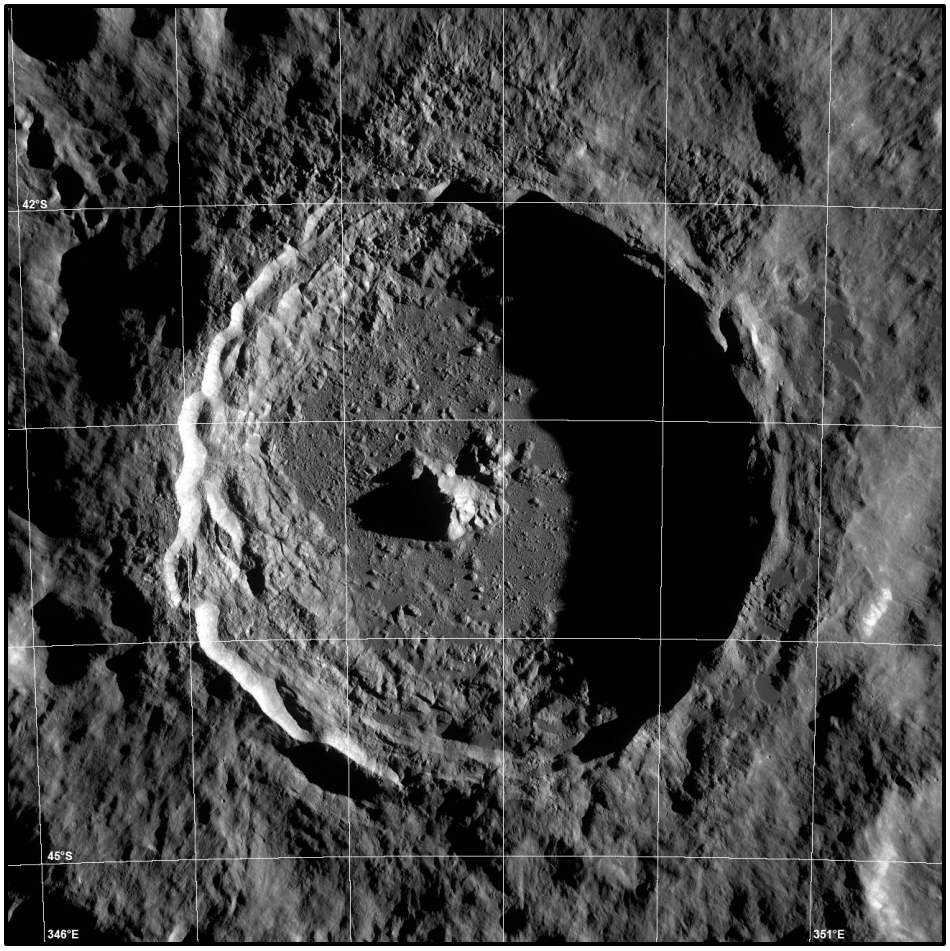

Figure 12. LROC WAC mosaic of Tycho crater. Image is 130 km wide [NASA/GSFC/Arizona State University].

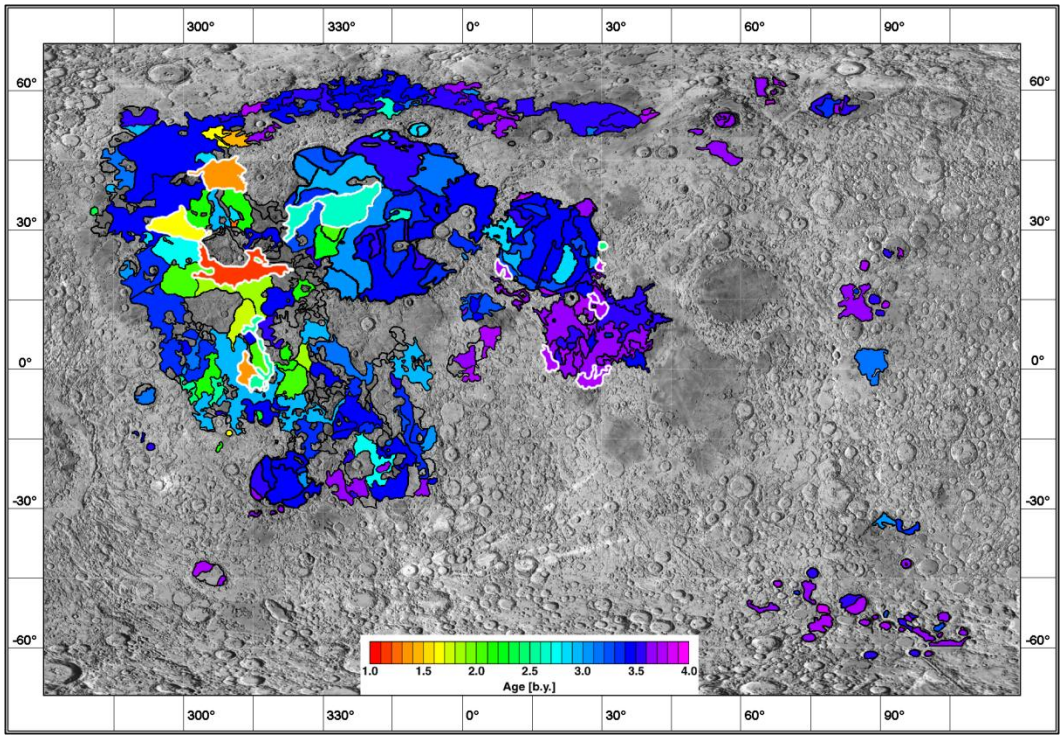

Figure 13. Color-coded map of lunar mare basalts using crater size-frequency distribution measurements. Oceanus Procellarum displays the widest range in ages, as well as the youngest units dated. All units define a single eruptive phase. Units outlined in white represent areas studied in this thesis. From Hiesinger et al., 2010.

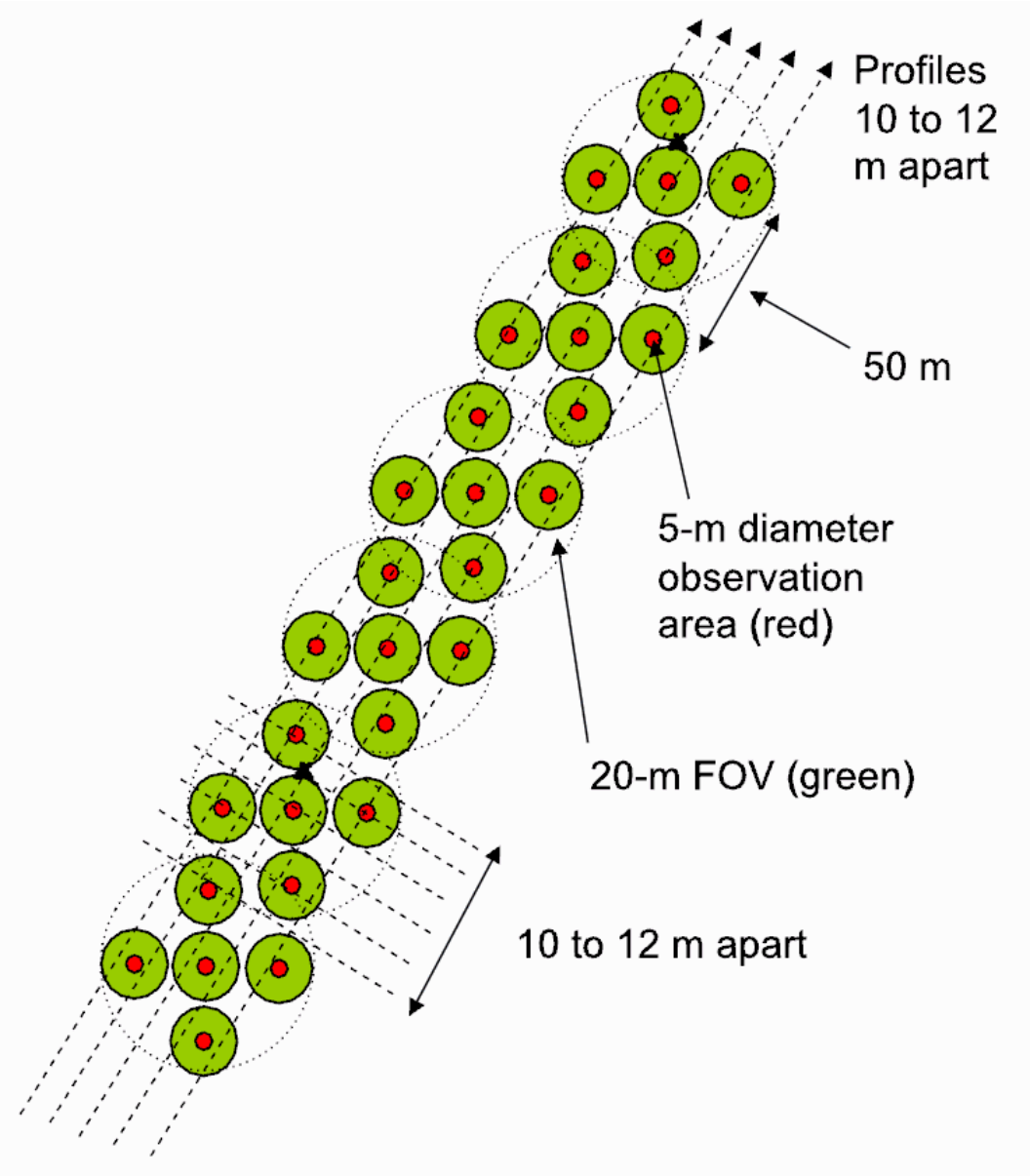

Figure 14. Schematic of LOLA five spot configuration. The red circle is the area illuminated by the laser, and the green circle is the field of view of each beam. From Smith et al., 2010b.

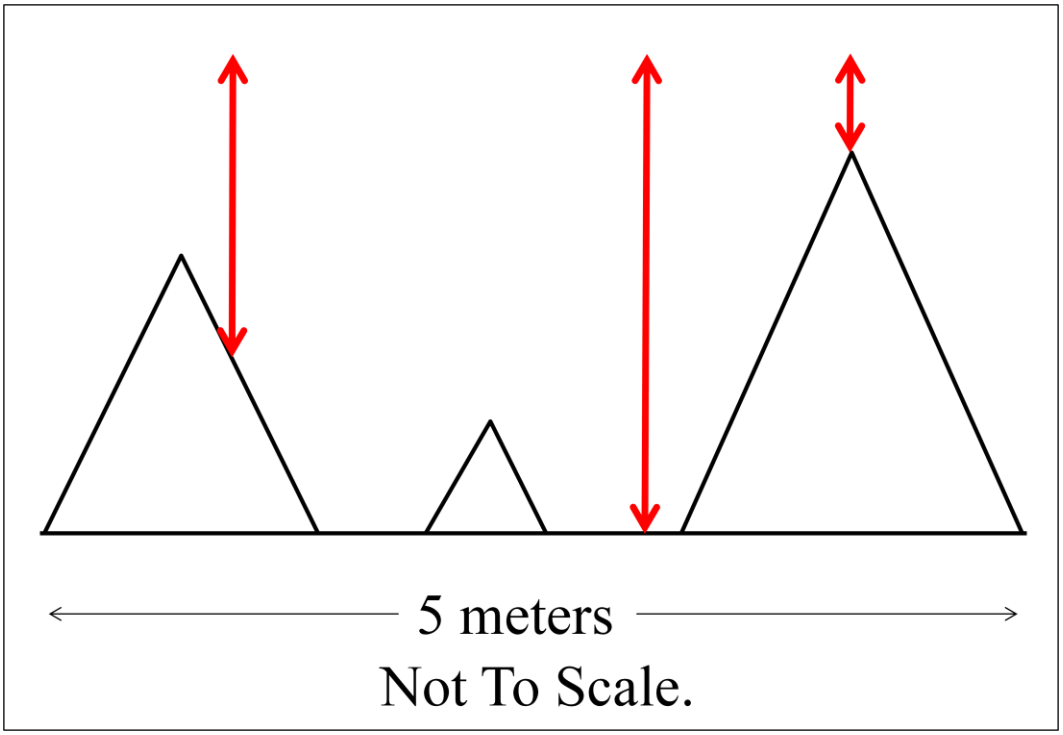

Figure 15. Schematic representing the spreading of a beam pulse in time due to surface roughness within each 5 m laser footprint. Rougher topography causes beam broadening to increase.

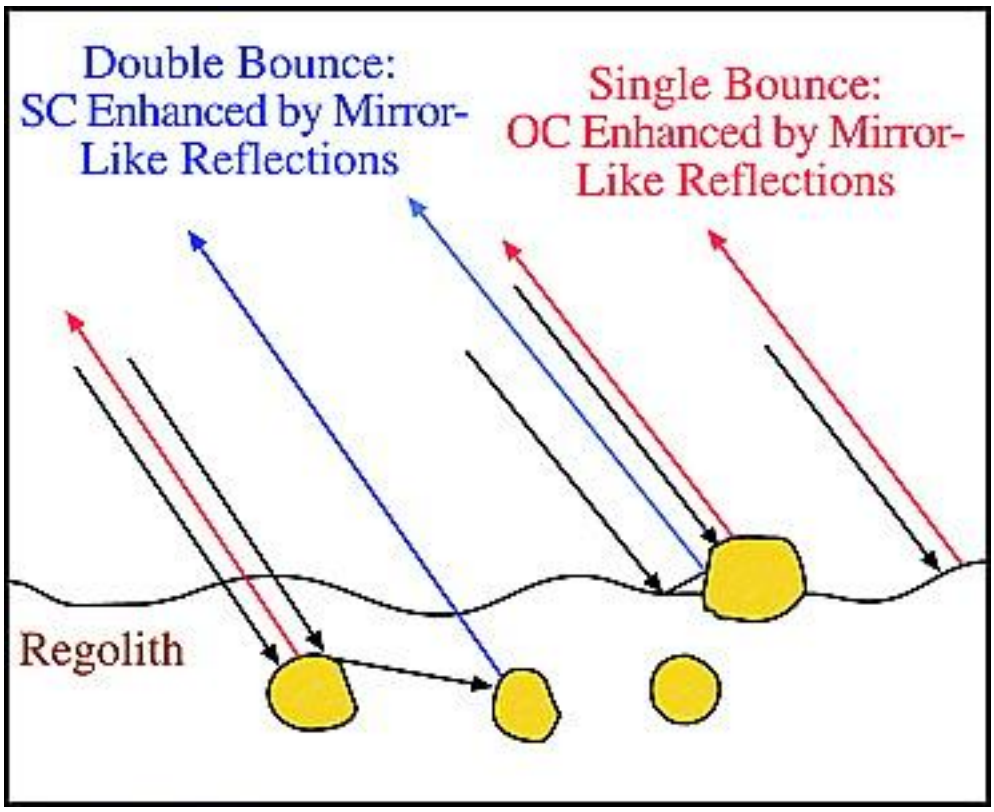

Figure 16. Schematic showing radar scattering with surface and suspended rocks. Black arrows represent incident radar signals; red arrows are OC echoes; blue arrows are SC echoes. Radar penetration depth correlates to the wavelength used, as well as regolith composition. From Campbell et al., 2009b.

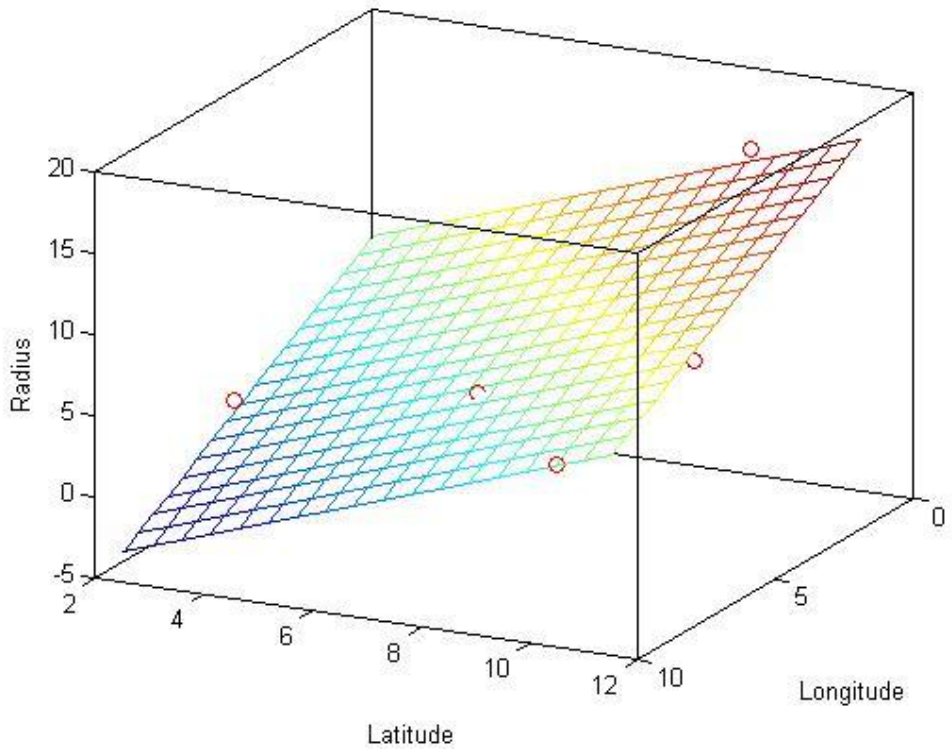

Figure 17. Schematic of Least-Squares Best Fit Plane. Created in MATLAB, this is a simulated dataset similar to those generated in almap.m. Note: this plot does not represent real altimetry data from LOLA.

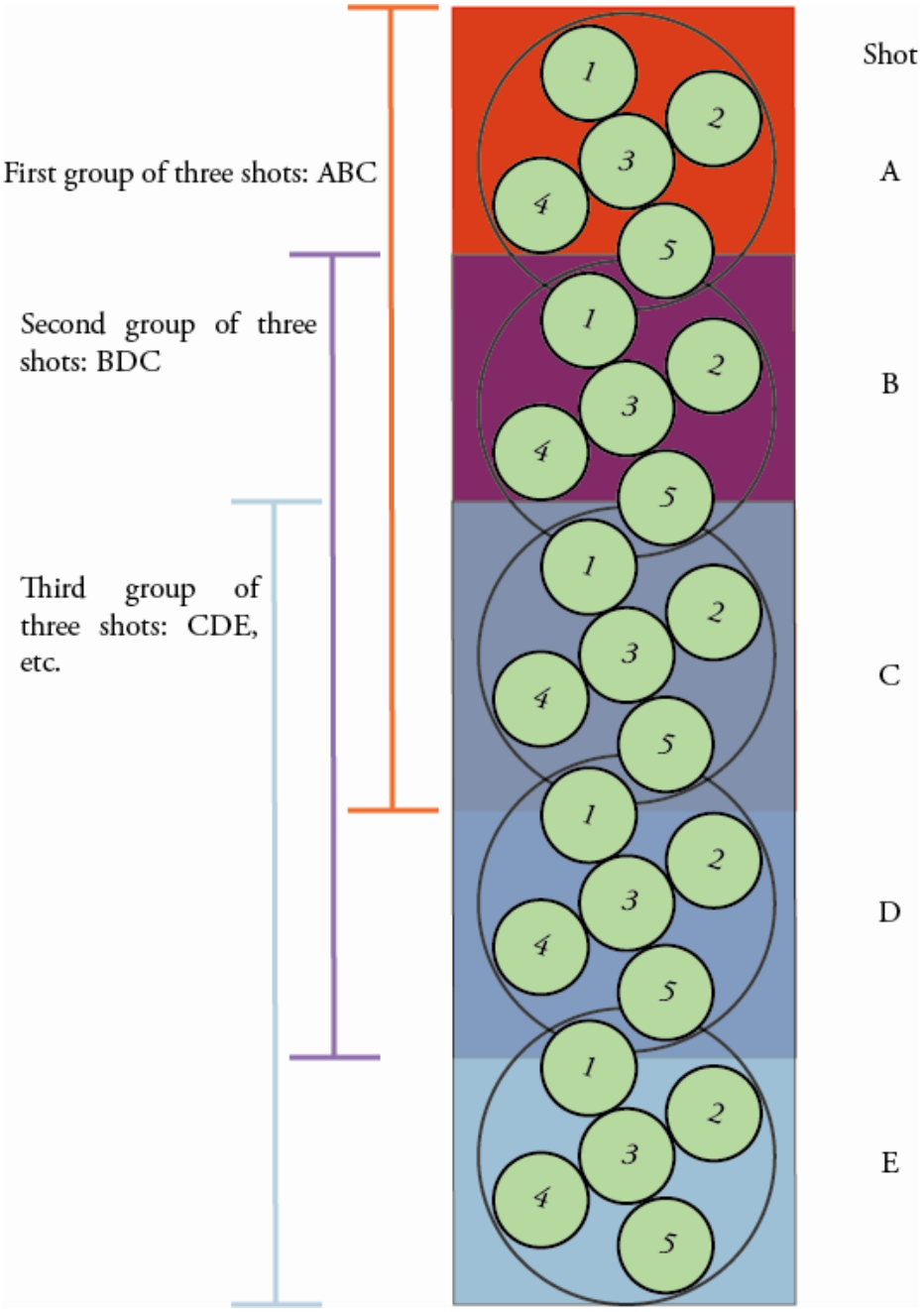

Figure 18. Grouping technique used in altmap.m. The first three shots are grouped together and analyzed; then, the second, third and fourth shots are grouped and analyzed; then the third, fourth and fifth are analyzed; and so on.

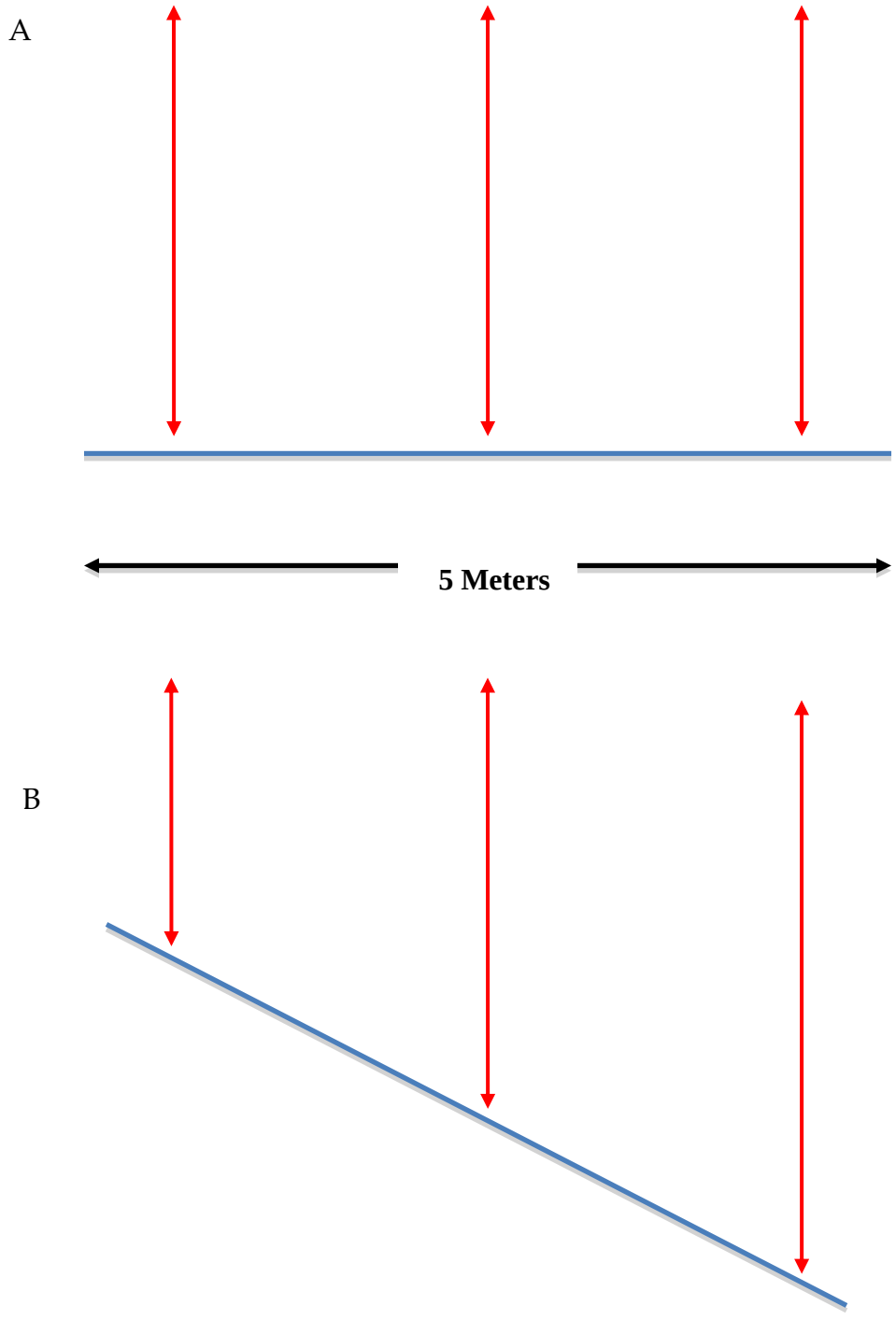

Figure 19. Schematic representing how slopes can affect pulse width returns. (A) Travel time of the beam remains constant over a surface with no slope. (B) Travel time varies when there is a slope across the 5 m observation area.

A

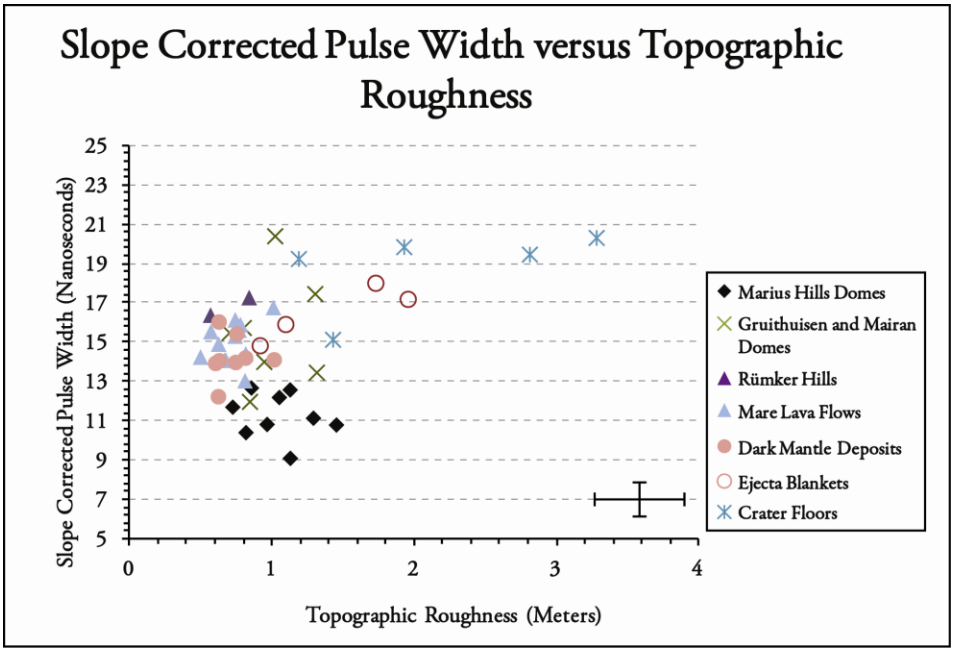

B

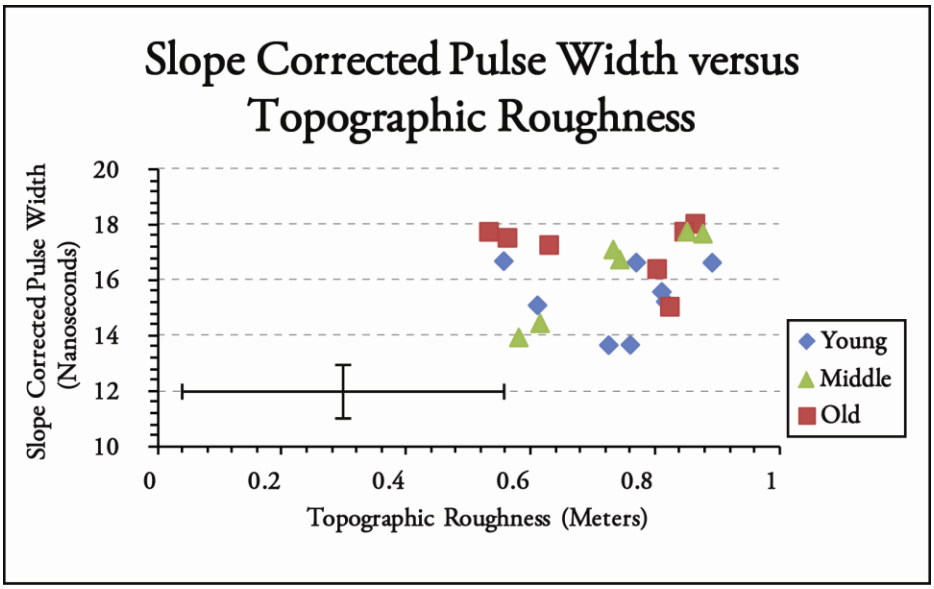

Figure 20. (A) Slope corrected pulse width versus topographic roughness for each study region. (B) Slope corrected pulse width versus topographic roughness for mare flows of varying ages. Young mare include flows with model absolute ages between 1.2-1.68 Ga. Middle mare include flows between 2.44-2.62 Ga. Old mare include flows between 3.75-3.81. Error bars in these and all following plots represent one-sigma ranges for each parameter. Note that these are a reflection of real variation on these surfaces rather than measurement uncertainties.

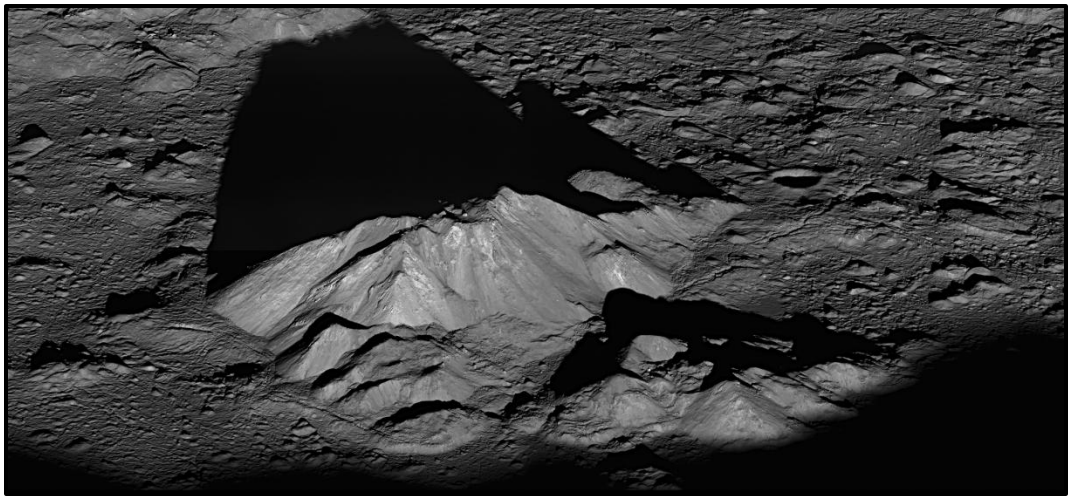

Figure 21. LROC NAC oblique view of Tycho's central peak complex. [NASA/GSFC/Arizona State University].

A

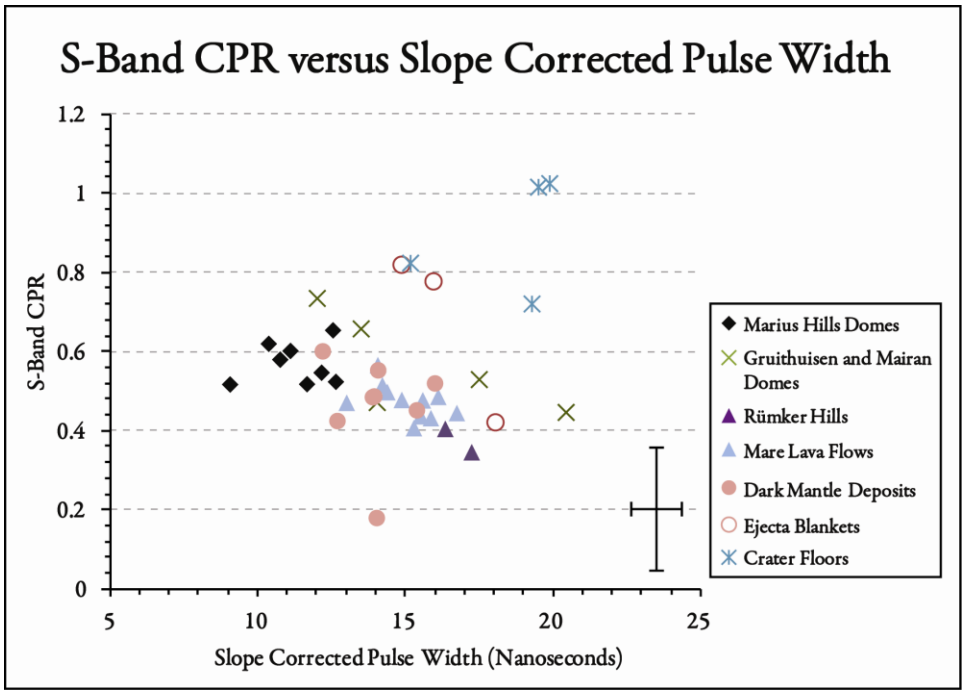

B

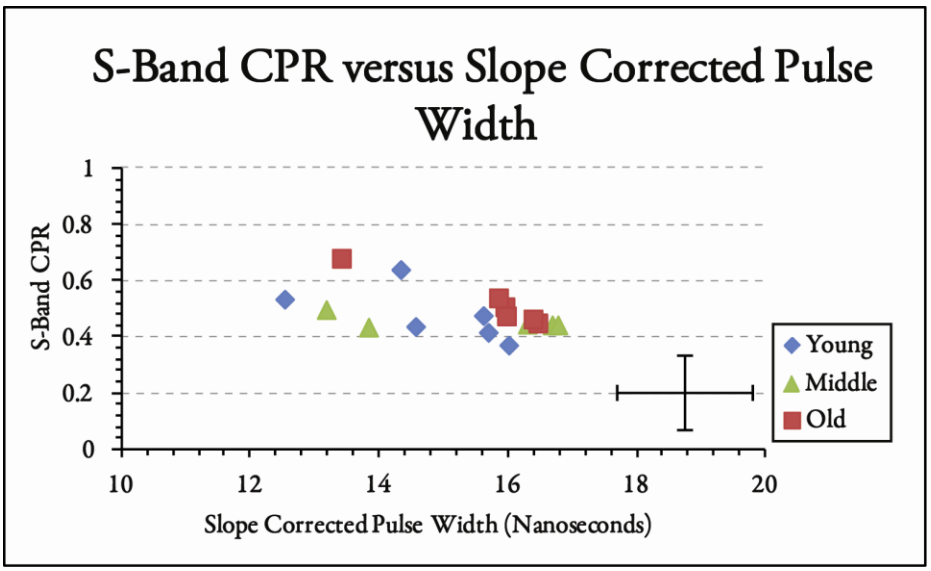

Figure 22. (A) S-Band CPR verses Slope Corrected Pulse Width for each study region. (B) S-Band CPR versus Slope Corrected Pulse Width for mare flows of varying ages.

A

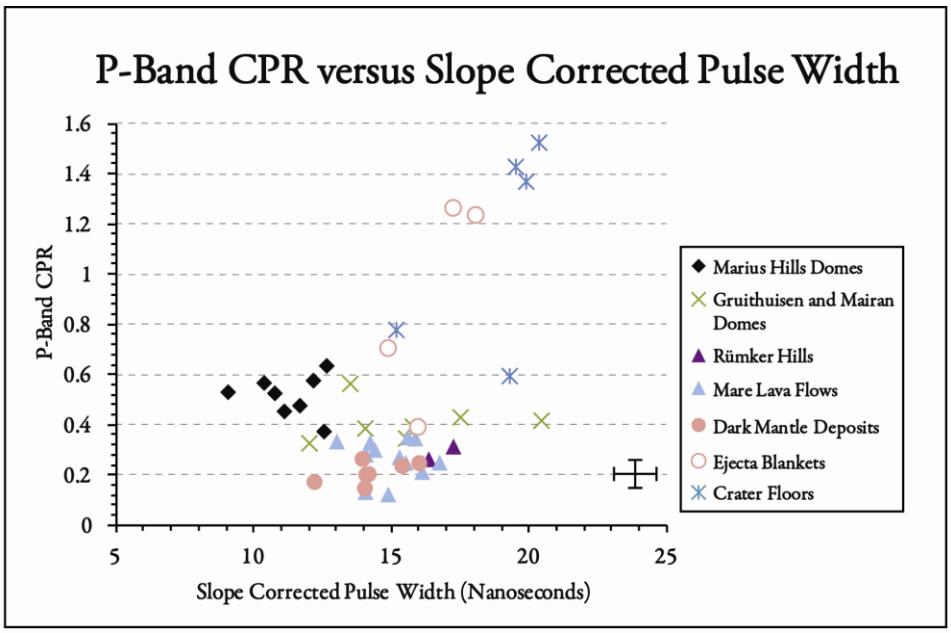

B

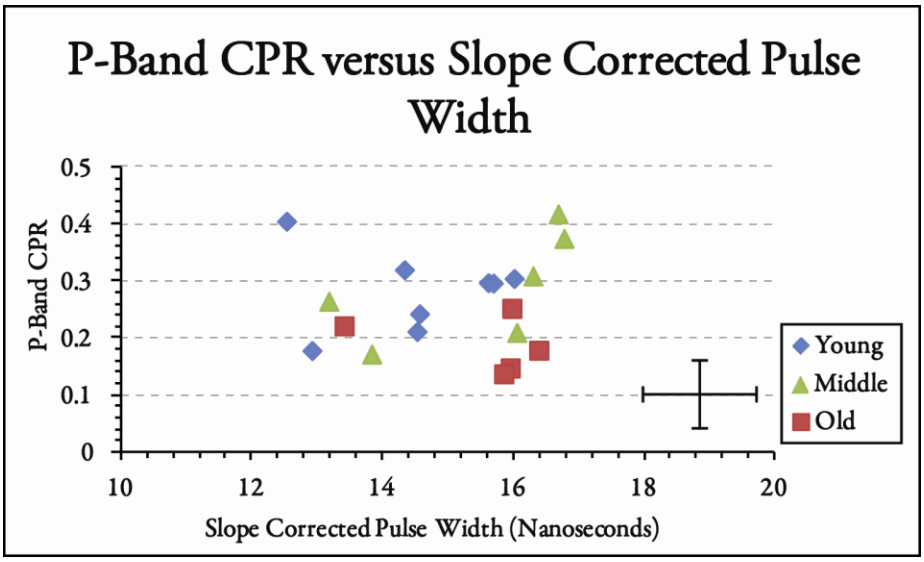

Figure 23. (A) P-Band CPR versus Slope Corrected Pulse Width for each study region. (B) P-Band CPR versus Slope Corrected Pulse Width for mare flows of varying ages.

A

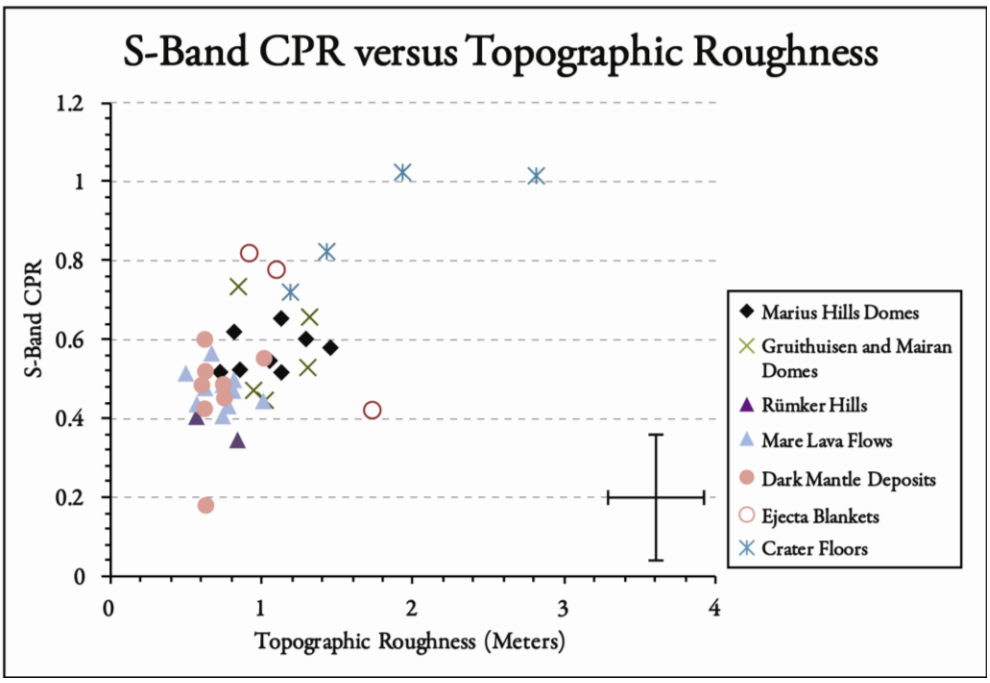

B

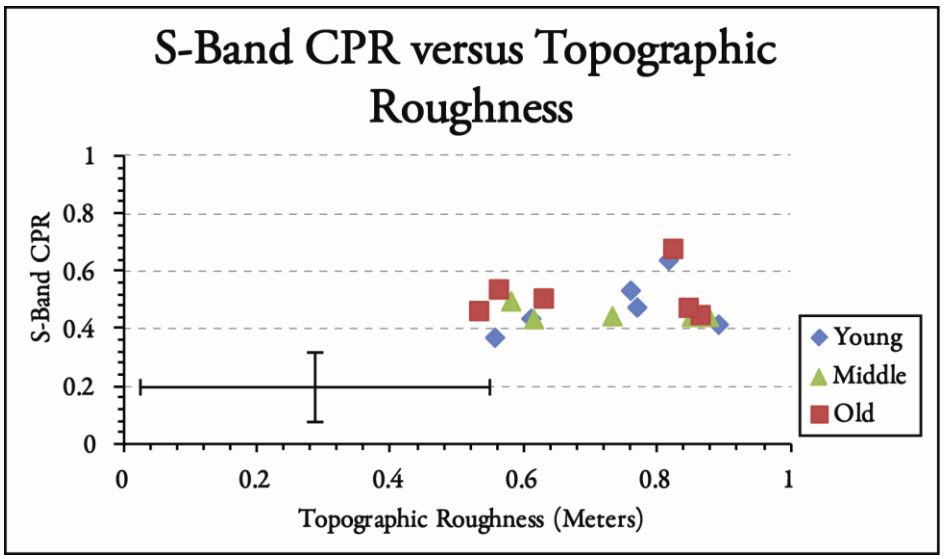

Figure 24. (A) S-Band CPR versus Topographic Roughness for each study region. (B) S-Band CPR versus Topographic Roughness for mare flows of varying ages.

A

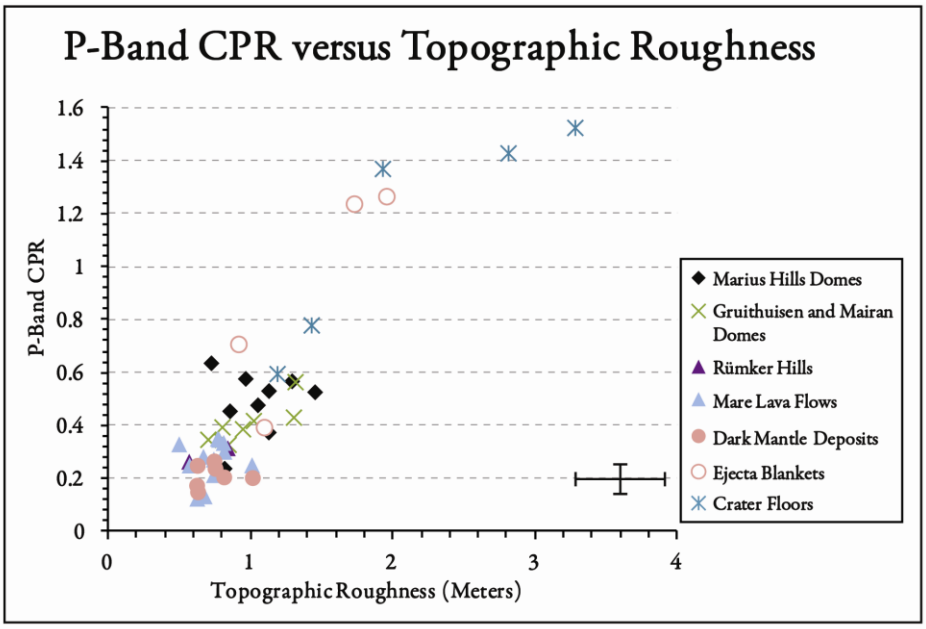

B

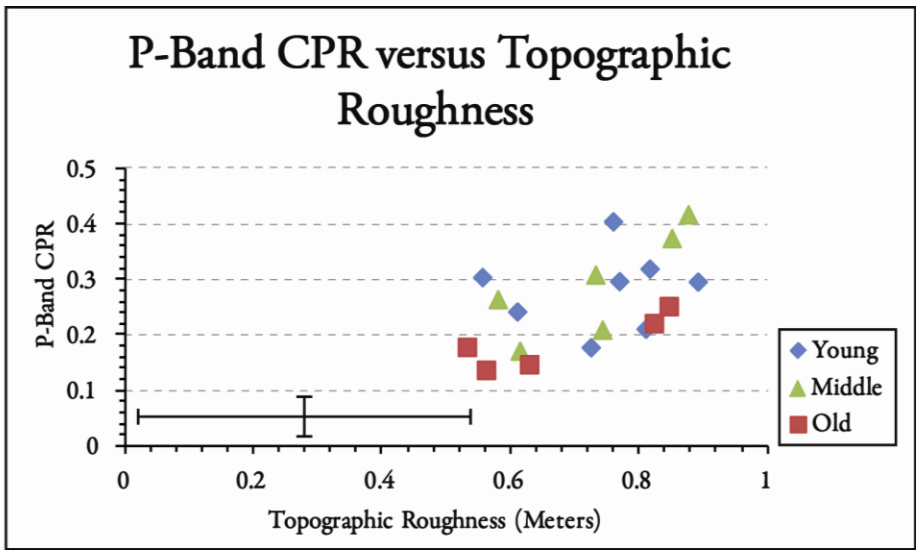

Figure 25. (A) P-Band CPR versus Topographic Roughness for each study region. (B) P-Band CPR versus Topographic Roughness for mare flows of varying ages.

A

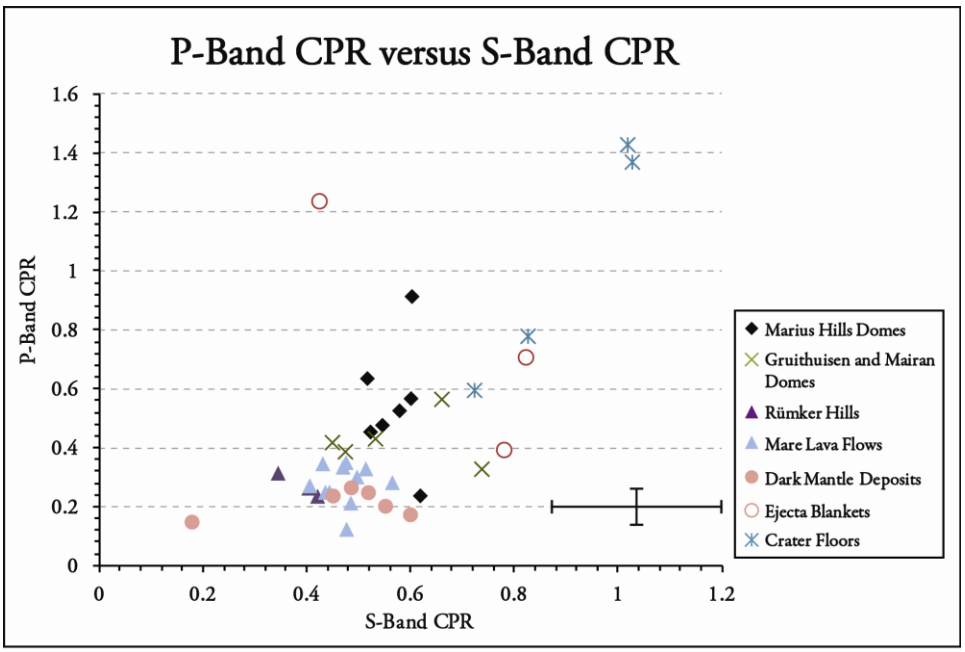

B

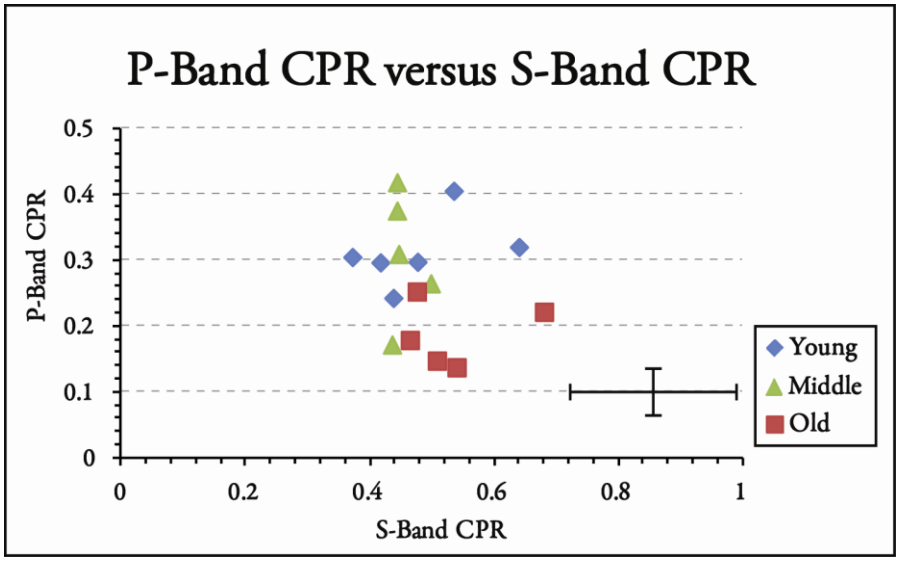

Figure 26. (A) P-Band CPR versus S-Band CPR for each study region. (B) P-Band CPR versus S-Band CPR for mare flows of varying ages.

A

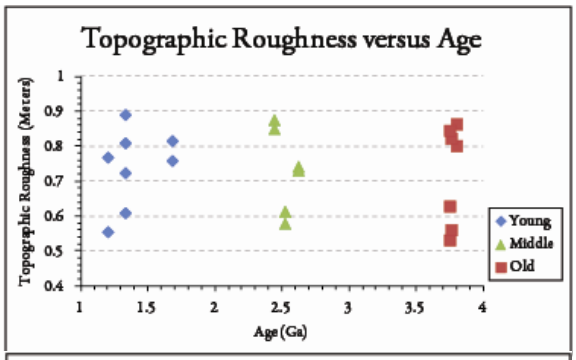

B

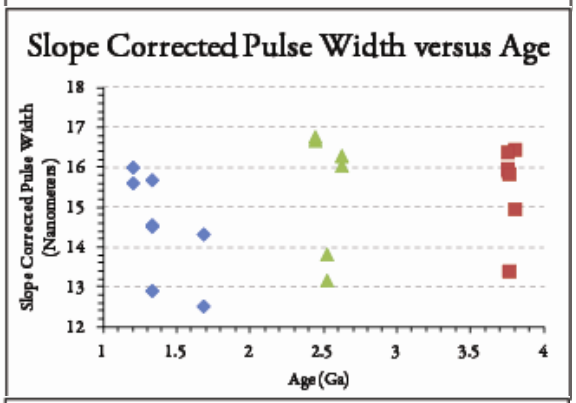

C

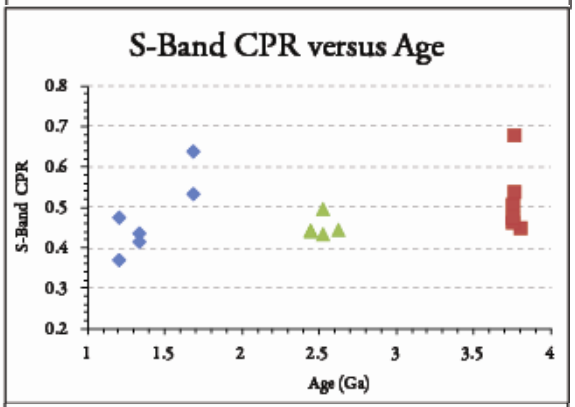

D

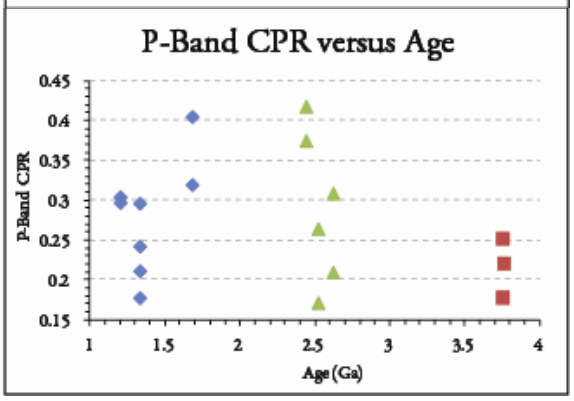

Figure 27. (A) through (D) plot surface roughness parameters against age for mare flows of varying ages.

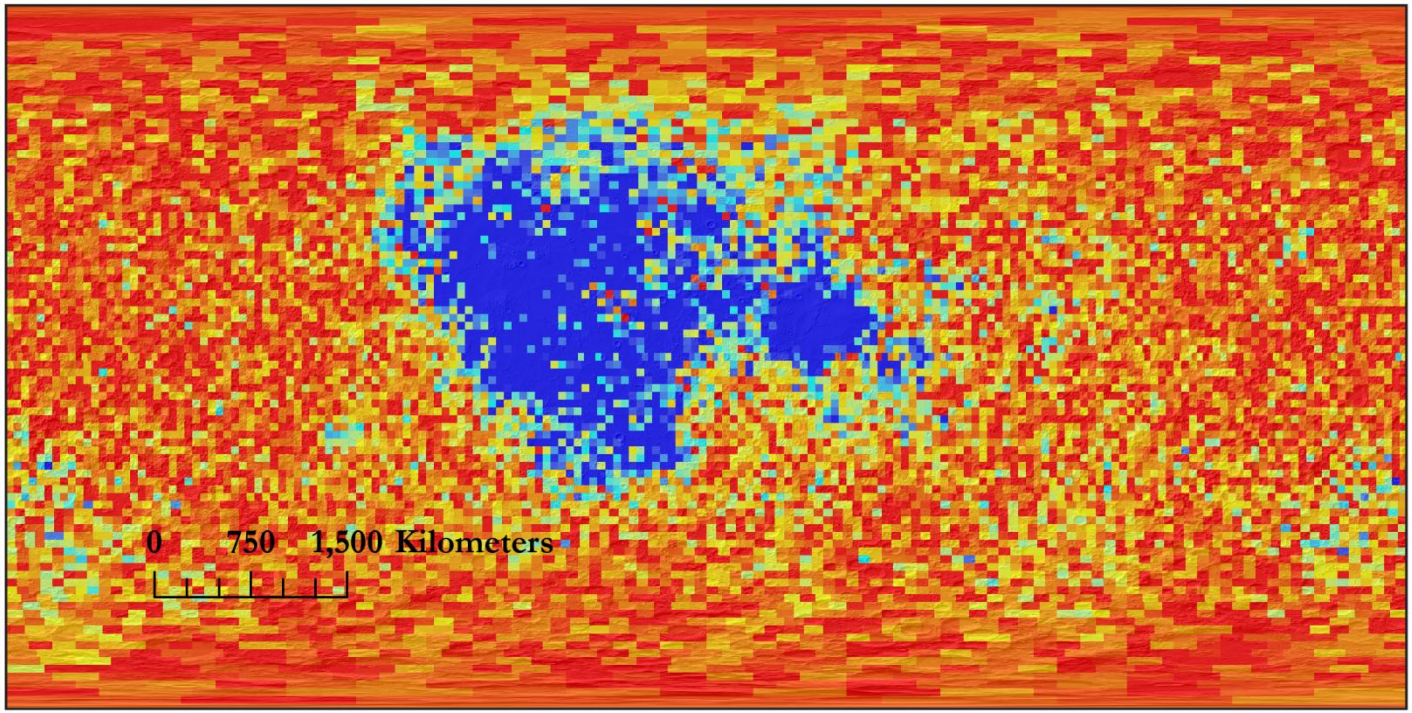

Figure 28. Map of titanium content across the lunar surface. Data from the Gamma Ray Spectrometer onboard the Lunar Prospector (Prettyman et al., 2006).

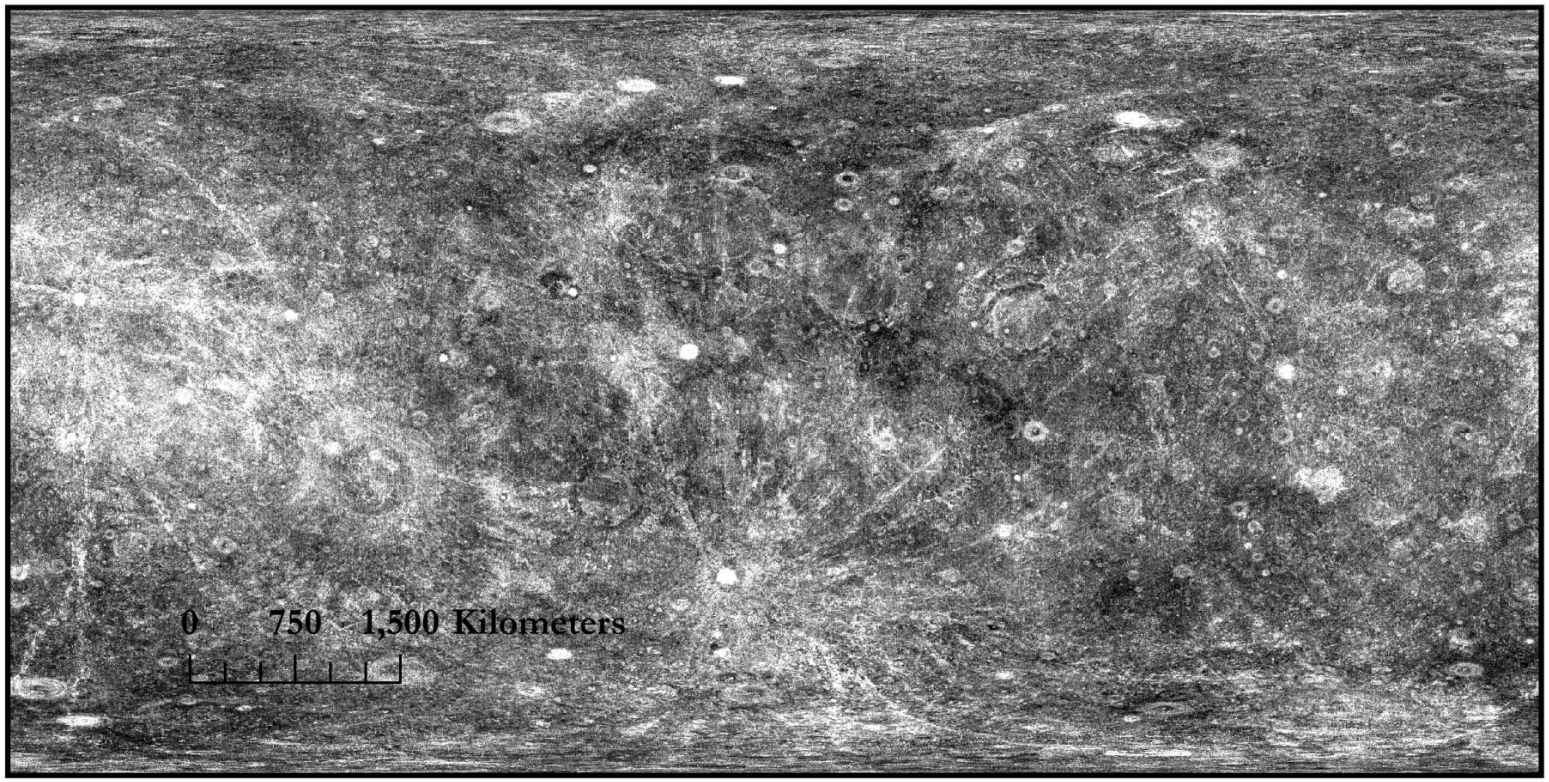

Figure 29. Global lunar roughness map derived from LOLA data. Note: this map only includes LOLA data through January 31, 2011. For more information see http://imbrium.mit.edu/DATA/LOLA_GDR/CYLINDRICAL/IMG/LDRM_16.LBL

APPENDIX

Appendix A.

```
%%%%%%%%%%%%%%%%%%%%%%%%%%%%%%%%%%%%%%%%%%%%%%
%ALTMAP.M, ERICA JAWIN, WRITTEN AT LPI, JUNE-AUGUST 2011
%SENIOR THESIS, DEPARTMENT OF ASTRONOMY, MOUNT
%HOLYOKE COLLEGE, SOUTH HADLEY, MA 2011-2012
%altmap imports data from a FramePerRow.csv file and creates a table of parameters for
%each of LOLA's five beams. Tables contain Lat, Long, Radius and Pulse Width. Valid
%data points are analyzed and inverted, and a three-dimensional plane will be fit to the
%data points to calculate slope of the lunar surface. RMS misfit, average pulse width and
%mean slope is then calculated. Histograms of RMS, mean slope and Pulse Width are
%created.

%%%%%%%%%%%%%%%%%%%%%%%%%%%%%%%%%%%%%%%%%%%%%%
%READ IN DATA FROM .CSV FILE AND CREATE MATRICES FOR LONG, LAT, RAD,
%AND PULSE WIDTH

%Look at data file and find all frames in a single orbit
clear
[Q F]=importdata('RDR_3E4E_34N35NFramePerRow_csv_table_.csv',',',1);
framelen=0;
zero=0;
use=0;
datasize=size(Q.data);
datalength=datasize(1);
for al=1:datalength
  if al==1
    frames1=1;
    for sal=al+1:datalength
      if abs(Q.data(sal,2)-Q.data(sal-1,2))<10
        if sal==datalength
          frames2=sal;
        else continue
        end
      elseif abs(Q.data(sal,2)-Q.data(sal-1,2))>10
        frames2=sal-1;
        break
      end
    end
  elseif al==datalength
    frames2=al;
```

```
      continue
   elseif abs(Q.data(al-1,2)-Q.data(al,2))>10
      frames1=al;
      for sal=al+1:datalength
         if abs(Q.data(sal,2)-Q.data(sal-1,2))<10
            if sal==datalength
               frames2=sal;
            else continue
            end
         elseif abs(Q.data(sal,2)-Q.data(sal-1,2))>10
            frames2=sal-1;
         break
         end
      end
   elseif abs(Q.data(al-1,2)-Q.data(al,2))<10
         continue
   end
framelen=frames2-frames1+1;

%Clear certain variables after each orbit has been analyzed
clear Long; clear Lat; clear Rad; clear PulseW; clear Flag; clear Colat; clear long_deg; …
clear colat_deg; clear x_Long; clear y_Colat; clear z_Rad; clear Orbit; clear Coordinates;…
clear points; clear C; clear Pulse; clear aa; clear GG; clear bb; clear DD; clear G; clear z;…
clear GTG; clear GTd; clear m; clear zero; clear hee; clear M; clear see; clear BB; clear…
sizem; clear Lou; clear Lout; clear theta; clear mslope; clear A1; clear B1; clear long1; …
clear colat1; clear rad1; clear long_rad; clear colat_rad; clear long2; clear olat2 clear …
rad2; clear mmloc; clear loc; clear wee; clear pow; clear pulse_width; clear location; …
clear Z; clear zeta; clear squared; clear Sum; clear meansquare; clear Rms; clear out;

%Make a matrix of the longitude measurements for each beam in an orbit
Long=zeros(framelen,5);
for i=frames1:frames2
   Long(i-(frames1-1),1)=Q.data(i,11);
   Long(i-(frames1-1),2)=Q.data(i,21);
   Long(i-(frames1-1),3)=Q.data(i,31);
   Long(i-(frames1-1),4)=Q.data(i,41);
   Long(i-(frames1-1),5)=Q.data(i,51);
end

%Make matrix of the latitude measurements for each beam in an orbit
Lat=zeros(framelen,5);
for i=frames1:frames2
   Lat(i-(frames1-1),1)=Q.data(i,12);
   Lat(i-(frames1-1),2)=Q.data(i,22);
```

```
   Lat(i-(frames1-1),3)=Q.data(i,32);
   Lat(i-(frames1-1),4)=Q.data(i,42);
   Lat(i-(frames1-1),5)=Q.data(i,52);
end

%Make matrix of the radius measurements for each beam in an orbit
Rad=zeros(framelen,5);
for i=frames1:frames2
   Rad(i-(frames1-1),1)=Q.data(i,13);
   Rad(i-(frames1-1),2)=Q.data(i,23);
   Rad(i-(frames1-1),3)=Q.data(i,33);
   Rad(i-(frames1-1),4)=Q.data(i,43);
   Rad(i-(frames1-1),5)=Q.data(i,53);
end

%Make matrix of the Pulse Width for each beam in an orbit
PulseW=zeros(framelen,5);
for i=frames1:frames2
   PulseW(i-(frames1-1),1)=Q.data(i,15);
   PulseW(i-(frames1-1),2)=Q.data(i,25);
   PulseW(i-(frames1-1),3)=Q.data(i,35);
   PulseW(i-(frames1-1),4)=Q.data(i,45);
   PulseW(i-(frames1-1),5)=Q.data(i,55);
end

%Makes matrix of the flag for each beam in an orbit. If flag=0, there is no
%error; if flag does not equal zero, ie 89,99 etc the data is unusable.
Flag=zeros(framelen,5);
for i=frames1:frames2
   Flag(i-(frames1-1),1)=Q.data(i,20);
   Flag(i-(frames1-1),2)=Q.data(i,30);
   Flag(i-(frames1-1),3)=Q.data(i,40);
   Flag(i-(frames1-1),4)=Q.data(i,50);
   Flag(i-(frames1-1),5)=Q.data(i,60);
end

%%%%%%%%%%%%%%%%%%%%%%%%%%%%%%%%%%%%%%%%%%%%%%%%%%%%%%%%%%%%%%%%%%%%%%%
%REMOVE UNUSABLE DATA VIA FLAGS AND CREATE MATRIX OF USABLE
%POINTS

%Convert Radius from km to m
Rad=Rad*1000;
```

```
%Convert from degrees to radians
long_rad=Long*(pi/180);
lat_rad=Lat*(pi/180);

x_Long=long_rad;
y_Lat=lat_rad;
z_Rad=Rad;

%Orbit contains Long, Lat, Rad, PulseW and Flag for each beam
Orbit=[Long(:,1) Lat(:,1) Rad(:,1) PulseW(:,1) Flag(:,1) ...
   Long(:,2) Lat(:,2) Rad(:,2) PulseW(:,2) Flag(:,2) ...
   Long(:,3) Lat(:,3) Rad(:,3) PulseW(:,3) Flag(:,3) ...
   Long(:,4) Lat(:,4) Rad(:,4) PulseW(:,4) Flag(:,4) ...
   Long(:,5) Lat(:,5) Rad(:,5) PulseW(:,5) Flag(:,5)];

%Coordinates contains the same parameters as Orbit in Radians
Coordinates=[x_Long(:,1) y_Lat(:,1) z_Rad(:,1) PulseW(:,1) Flag(:,1) ...
   x_Long(:,2) y_Lat(:,2) z_Rad(:,2) PulseW(:,2) Flag(:,2) ...
   x_Long(:,3) y_Lat(:,3) z_Rad(:,3) PulseW(:,3) Flag(:,3) ...
   x_Long(:,4) y_Lat(:,4) z_Rad(:,4) PulseW(:,4) Flag(:,4) ...
   x_Long(:,5) y_Lat(:,5) z_Rad(:,5) PulseW(:,5) Flag(:,5)];

%Create matrix of valid points.
clear A;clear B;
format long
points=0;
for q=1:framelen-2
   for pp=q:q+2
      for b=5:5:25;
         if Coordinates(pp,b)==0;
            points=points+1;
%B Matrix contains valid data points (Flag=0). Coordinates(pp,b-4) is Longitude;
%Coordinates(pp,b-3) is Latitude; Coordinates(pp,b-2) is Radius; Coordinates(pp,b-1) is
%Pulse Width
          B(points,:)=[Coordinates(pp,b-4) Coordinates(pp,b-3) ...
             Coordinates(pp,b-2) Coordinates(pp,b-1)];
         end
      end
   end

%Create Matrix A, containing same parameters as Matrix B. All valid points in a group of
%3 frames have been subtracted from the first data point.
   if q==1
      for pq=1:points
```

```
        for j=1:3
            A(pq,j)=B(pq,j)-B(1,j);
        end
    end
  else rl=length(A);
    for pr=rl+1:points
        for j=1:3
            A(pr,j)=B(pr,j)-B(rl+1,j);
        end
    end
  end
end
meanrad=1737400;
for i=1:points
  for j=1:2
    A(i,j)=A(i,j)*meanrad;
  end
end

C=B;
C(:,1:2)=(180/pi)*(B(:,1:2));
C(:,5:7)=A(:,:);

%%%%%%%%%%%%%%%%%%%%%%%%%%%%%%%%%%%%%%%%%%%%%%%%%%%%%%%%%%%%%%%%%%%%%%%%%%%%%%%%
%CREATE LEAST SQUARES PLANE TO FIT TO DATA POINTS IN MATRIX A

%Count the number of valid data points, bb, for each set of 3 frames, and create matrix
%DD containing all values of bb
for ri=1:points
  if A(ri,1)==0
    aa=ri;
    for gg=ri+1:points
        GG=gg;
        bb=(GG-aa);
        if A(gg,1)==0
            break
        end
        if gg==points
            bb=(points-ri+1);
            continue
        end
        if A(gg,1)~=0
            continue
        end
```

```
        end
        DD(ri,1)=bb;
        if bb <9
            continue
        end

%Use least-squares method to fit a plane surface to the set of data points
        G=ones(bb,3);
        z=A(ri:bb+ri-1,3);
        for ee=1:bb
            for k=1:2
                G(ee,k+1)=A(ee+ri-1,k);
            end
        end
        GTG=G'*G;
        GTd=G'*z;
        m(ri,:)=[inv(GTG)*GTd]';
    end
end

%Remove 0's from matrix DD and create matrix BB
see=0;
for xx=1:length(DD)
    if DD(xx)~=0
        see=see+1;
        BB(see,1)=DD(xx);
    end
end
bsize=size(BB);blength=bsize(1);

%Create message for if each orbit contains enough data to produce valid results
if sum(BB)<9*blength
    fprintf('ERROR: NOT ENOUGH POINTS TO CREATE VALID… RESULTS\n')
    continue
    elseif sum(BB)>=9*blength
    fprintf('CONGRATULATIONS! THERE ARE ENOUGH POINTS TO… CREATE
VALID RESULTS\n')
end

%Remove 0's from matrix m and create matrix M
hee=0;
for ii=1:length(m)
    if m(ii,1)||m(ii,2)||m(ii,3)~=0
        hee=hee+1;
```

```
      M(hee,:)=m(ii,:);
   end
end

%%%%%%%%%%%%%%%%%%%%%%%%%%%%%%%%%%%%%%%%%%%%%%%%%%%%%%%%%%%%%%%%%%%%%%%%
%CALCULAE RMS MISFIT CALCULATING RMS MISFIT
%Z(~)=Ax+By+C ---> m(2)x+m(3)y+m(1)=Z(~)

%Matrix Z contains predicted values to calculate RMS misfit
%Z is the matrix of Ax+By+C=Z(~) values, zeta is the matrix of Z(~)-Z values

location=0;
for mm=1:length(m)
   if m(mm,1)||m(mm,2)||m(mm,3)~=0
      location=location+1;
      for quant=1:DD(mm) %DD(mm) is the number of valid points in each frame
         Z(quant,location)=m(mm,2)*A(mm+quant-1,1)+m(mm,3)*A(mm+quant-…
1,2)+m(mm,1);
         zeta(quant,location)=Z(quant,location)-A(mm+quant-1,3);
      end
      squared=zeta.^2;
      Sum(location)=sum(squared(:,location),1);
      meansquare(:,location)=Sum(location)/DD(mm);
      Rms(location,1)=sqrt(meansquare(:,location));
   end
end

%%%%%%%%%%%%%%%%%%%%%%%%%%%%%%%%%%%%%%%%%%%%%%%%%%%%%%%%%%%%%%%%%%%%%%%%
%CALCULATING MEAN SLOPE Ax+By+D=Cz --> m(2)+m(3)+m(1)=z

%Values for A1, B1, C1 are taken from M matrix
%Horizontal plane is created under parameters A2=0, B2=0, C2=-1
%acos function returns values in radians, while the mslope matrix converts these values
%to degrees

sizem=size(M);
lenm=sizem(1);

theta=zeros(lenm,1);
for hh=1:lenm
   A1=M(hh,2);
   B1=M(hh,3);
   C1=-1;
   A2=0;
```

```
   B2=0;
   C2=-1;
   theta(hh)=acos(abs(A1*A2+B1*B2+C1*C2)/((sqrt(A1^2+B1^2+C1^2)*…
sqrt(A2^2+B2^2+C2^2))));
end
mslope=(180/pi)*(theta);

%%%%%%%%%%%%%%%%%%%%%%%%%%%%%%%%%%%%%%%%%%%%%%%%%%%%%%%%%%%%%%%%
%CALCULATE AVERAGE PULSE WIDTH

%Pulse Width is averaged over each set of frames in an orbit
Pulse=B(:,4);
wee=0;
for pw=1:length(DD)
   if DD(pw)~=0
      wee=wee+1;
      pow=pw+DD(pw)-1;
      pulse_width(wee,1)=mean(Pulse(pw:pow));
   end
end

%%%%%%%%%%%%%%%%%%%%%%%%%%%%%%%%%%%%%%%%%%%%%%%%%%%%%%%%%%%%%%%%
%CREATE OUTPUT MATRIX WITH PARAMETERS [LONG, LAT, RAD, A, B, C,
%POINTS, RMS, MEAN SLOPE, PULSE WIDTH]. FOR EACH SET OF 3 FRAMES
%CREATE USABLE MATRIX WHICH CONTAINS OUTPUT MATRIX DATA IF THERE
%ARE MORE THAN 9 DATA POINTS PER ORBIT

c=0;
Out=zeros(1,10);
for i=1:length(m)
   if C(i,5:7)==[0 0 0]
      for c=1:lenm
      Out(c,1:13)=[C(i,1) C(i,2) C(i,3) M(c,2) M(c,3) M(c,1) BB(c,1) ...
      Rms(c) mslope(c) pulse_width(c)];
      end
   end
end
out=size(Out);
for sa=1:out(1)
   if Out(sa,7)>8
      use=use+1;
      usable(use,:)=Out(sa,:);
   end
end
```

```
%END OF 1 ORBIT.
end

%1-Dimensional arrays are created from usable matrix for ease of viewing
Longitude=usable(:,1);
Latitude=usable(:,2);
Radius=usable(:,3);
A_m=usable(:,4);
B_m=usable(:,5);
C_m=usable(:,6);
Points=usable(:,7);
RMS=usable(:,8);
Mean_Slope=usable(:,9);
Pulse_Width=usable(:,10);
mean_rms=mean(RMS);
srms=std(RMS);
mean_meanslope=mean(Mean_Slope);
sms=std(Mean_Slope);
mean_pwidth=mean(Pulse_Width);
spw=std(Pulse_Width);
params=[mean_rms srms mean_meanslope sms mean_pwidth spw];

%%%%%%%%%%%%%%%%%%%%%%%%%%%%%%%%%%%%%%%%%%%%%%%%%%%%%%%%%%%%%%%%%%%%%%%%%%%%
%CREATE HISTOGRAMS, OUTPUT FILE

%Histograms of RMS, Pulse Width and Mean Slope are created using data from the
%usable matrix
clf; hist(RMS);
xlabel('RMS (meters)')
h=findobj(gca,'Type','patch');
set(h,'FaceColor','r','EdgeColor','w')

figure;hist(Pulse_Width);
xlabel('Pulse Width (nanoseconds)')
h=findobj(gca,'Type','patch');
set(h,'FaceColor','g','EdgeColor','w')

figure;hist(Mean_Slope);
xlabel('Mean Slope (degrees)')
h=findobj(gca,'Type','patch');
set(h,'FaceColor','b','EdgeColor','w')

%Excel file is created containing data from the usable matrix
xlswrite('Output.csv',usable); xlswrite('params.csv',params);
```

Feature	Long	Lat	Topographic Roughness	St Dev TR	Pulse Width	St Dev PW	Slope Corrected PW	S CPR	St Dev S CPR	P CPR	St Dev P CPR
MH Dome 1	301.36	11.71	1.13	0.69	14.94	0.85	9.07	0.52	**0.29**	0.53	0.22
MH Dome 2	303.09	12.46	1.13	0.95	15.34	1.02	12.56	0.65	0.41	0.37	0.09
MH Dome 3	304.52	13.09	1.46	0.94	15.31	1.03	10.77	0.58	0.37	0.52	0.17
MH Dome 4	304.74	14.00	N/A	N/A	N/A	N/A	N/A	0.60	0.40	0.91	0.18
MH Dome 5	305.51	12.16	0.97	0.50	14.20	0.49	10.80	N/A	N/A	0.58	0.18
MH Dome 6	305.66	11.61	1.05	0.50	14.87	0.48	12.17	0.55	0.39	0.48	0.14
MH Dome 7	305.75	14.71	0.73	0.41	14.21	0.45	11.68	0.52	0.32	0.63	0.19
MH Dome 8	306.21	11.80	0.86	0.45	14.80	0.68	12.66	0.52	0.34	0.45	0.13
MH Dome 9	306.42	14.81	1.29	0.96	15.29	0.86	11.12	0.60	0.39	0.57	0.23
MH Dome 10	307.63	11.79	0.82	0.50	15.22	0.75	10.38	0.62	0.38	0.24	0.05
Gruith d side	320.34	35.87	0.94	0.34	24.37	2.91	14.02	0.47	0.29	0.39	0.09
Gruith d top	320.34	36.08	1.30	0.87	22.71	2.16	17.48	0.53	0.31	0.43	0.10
Gruith g side	319.54	36.49	0.84	0.41	19.86	2.48	11.99	0.74	0.41	0.33	0.09
Gruith g top	319.21	36.56	1.02	0.75	23.75	2.05	20.42	0.45	0.29	0.42	0.12
Mairan top	311.60	41.79	1.31	0.73	24.28	2.25	13.48	0.66	0.37	0.57	0.10
Mairan middle	312.23	41.36	0.80	0.39	21.06	2.13	15.75	N/A	N/A	0.40	0.13
Mairan bottom	312.30	40.80	0.70	0.36	17.79	1.49	15.50	N/A	N/A	0.35	0.11
Rümker 1	301.40	40.96	0.84	0.48	18.91	1.52	17.26	0.35	0.19	0.31	0.07
Rümker 2	302.19	40.31	N/A	N/A	N/A	N/A	N/A	0.42	0.23	0.23	0.09
Rümker 3	301.31	40.10	0.57	0.37	18.25	2.32	16.36	0.40	0.22	0.26	0.08
Oceanus 1	298.84	24.32	0.78	0.55	16.71	1.41	15.87	0.43	0.23	0.35	0.07
Oceanus 2	304.92	0.00	0.57	0.48	16.38	1.67	15.52	0.44	0.25	0.25	0.11

Feature	Long	Lat	Topographic Roughness	St Dev TR	Pulse Width	St Dev PW	Slope Corrected PW	S CPR	St Dev S CPR	P CPR	St Dev P CPR
Oceanus 3	301.11	18.27	0.77	0.64	16.39	1.32	15.60	0.48	0.24	0.35	0.06
Imbrium 1	340.10	37.10	0.82	0.56	15.37	0.44	14.40	0.50	0.27	0.30	0.08
Imbrium 2	335.19	35.92	1.01	0.75	17.84	2.11	16.75	0.44	0.24	0.25	0.10
Imbrium 3	331.28	36.49	0.74	0.60	16.97	1.75	16.12	0.49	0.26	0.21	0.07
MH Plains 1	304.65	11.97	0.81	0.77	14.30	2.75	13.02	0.47	0.30	0.33	0.10
MH Plains 2	307.04	12.30	0.74	0.44	16.55	1.28	15.30	0.41	0.24	0.27	0.05
MH Plains 3	302.73	13.22	0.67	0.44	15.09	0.35	14.08	0.57	0.35	0.28	0.06
Serenitatis 1	25.63	15.76	0.68	0.44	15.92	2.10	14.06	N/A	N/A	0.13	0.03
Serenitatis 2	21.88	13.53	0.63	0.51	16.32	2.10	14.89	0.48	0.26	0.12	0.03
Serenitatis 3	27.79	12.86	0.50	0.25	15.35	0.72	14.23	0.51	0.28	0.33	0.14
Aestuum 1	345.36	6.54	1.02	0.77	18.25	4.55	14.09	0.55	0.31	0.20	0.06
Aestuum 2	350.72	6.67	0.63	0.40	17.01	1.56	16.01	0.52	0.28	0.25	0.04
Aestuum 3	335.71	11.63	0.82	0.54	16.26	0.51	14.18	N/A	N/A	0.20	0.05
Sulpicius 1	8.67	21.15	0.63	0.24	17.36	1.15	14.04	0.18	0.42	0.15	0.04
Sulpicius 2	8.68	21.85	0.63	0.33	17.30	1.46	12.21	0.60	0.32	0.17	0.04
Sulpicius 3	7.51	21.72	0.75	0.52	18.26	1.23	13.95	0.49	0.28	0.26	0.10
Vaporum 1	5.14	17.63	0.76	0.51	18.86	1.60	15.40	0.45	0.24	0.24	0.06
Vaporum 2	5.21	11.19	0.61	0.31	16.15	2.89	13.91	0.48	0.26	0.08*	0.02*
Vaporum 3	7.21	12.27	0.62	0.47	14.65	2.53	12.71	0.42	0.23	0.08*	0.02*
Copern Blank 1	337.50	9.50	1.09	0.76	20.73	1.30	15.93	0.78	0.42	0.39	0.16
Copern Blank 2	342.01	10.85	0.91	0.51	19.10	3.88	14.85	0.82	0.44	0.71	0.16
Tycho Blank 1	348.56	-41.45	1.95	1.20	23.93	2.54	17.21	N/A	N/A	1.27	0.32

Feature	Long	Lat	Topographic Roughness	St Dev TR	Pulse Width	St Dev PW	Slope Corrected PW	S CPR	St Dev S CPR	P CPR	St Dev P CPR
Tycho Blank 2	349.84	-41.85	1.73	0.98	22.21	2.24	18.03	0.42	0.24	1.24	0.27
Copern Floor 1	339.84	10.26	1.18	0.78	20.89	5.06	19.27	0.72	0.39	0.60	0.17
Copern Floor 2	340.91	9.85	1.43	0.83	22.84	3.76	15.15	0.83	0.44	0.78	0.23
Tycho Floor 1	349.40	-43.50	2.81	1.63	22.03	1.42	19.49	1.02	0.53	1.43	0.41
Tycho Floor 2	349.40	-43.02	1.93	1.13	21.25	0.96	19.87	1.03	0.53	1.37	0.23
Tycho Floor 3	349.23	-43.64	3.28	2.06	23.58	2.21	20.33	N/A	N/A	1.53	0.25

Appendix B. Table of roughness data collected for each lunar feature. Long/Lat are the central point of each feature, about which the 0.2 x 0.2° boxes were drawn. Units are as follows: Long/Lat values are in degrees; Topographic Roughness values are in meters; Pulse Width values are in nanoseconds; CPR values are dimensionless. Standard deviation values for Topographic Roughness (TR) and Pulse Width (PW) were calculated in altmap.m (see Appendix A). Standard deviation values for S- and P-band CPR values were calculated in ArcMap. MH Domes 1-10 are domes from the Marius Hills; Gruith g/d top and side, and Mairan top, middle and bottom are the Gruithuisen and Mairan domes, according to names assigned in the literature (see Figure 4 and 7). Rümker 1-3 are areas on the Rümker Hills. Oceanus 1-3 and Imbrium 1-3 are mare units from Oceanus Procellarum and Mare Imbrium, while MH Plains 1-3 are areas of the mare between the domes in the Marius Hills. Serenitatis 1-3 are areas of Mare Serenitatis. Aestuum 1-3, Sulpicius 1-3 and Vaporum 1-3 are dark mantle deposits as defined by Weitz & Head, 1999 (see Figure 9). Copern Blank 1-2 and Tycho Blank 1-2 are areas of the ejecta blankets around both craters, while Copern Floor 1-2 and Tycho Floor 1-3 are areas on the crater floors. N/A indicates no data in a particular parameter for a given feature. * Starred values may have been affected by edge brightening in the radar data.

Mare	Age	Long	Lat	Topographic Roughness	St Dev TR	Pulse Width	St Dev PW	Slope Corrected PW	S CPR	St Dev S CPR	P CPR	St Dev P CPR
P60	1.20	309.70	19.78	0.56	0.37	16.72	2.14	16.01	0.37	0.20	0.30	0.09
P60	1.20	312.38	20.53	0.77	0.51	16.67	1.54	15.61	0.48	0.25	0.30	0.09
P58	1.33	310.81	42.11	0.61	0.35	15.12	2.84	14.56	0.44	0.26	0.24	0.05
P58	1.33	310.45	40.24	0.89	0.76	16.66	2.55	15.69	0.42	0.22	0.30	0.10
P53	1.68	298.08	29.70	0.76	0.55	13.70	3.58	12.53	0.53	0.28	0.40	0.08
P53	1.68	301.35	30.28	0.82	0.61	15.25	1.76	14.33	0.64*	0.33*	0.32	0.08
P57	1.33	313.89	-1.84	0.72	0.55	13.69	3.10	12.92	N/A	N/A	0.18	0.06
P57	1.33	314.15	-0.16	0.81	0.92	15.61	1.28	14.52	N/A	N/A	0.21	0.06
I28	2.62	335.81	35.00	0.74	0.53	16.77	1.48	16.05	N/A	N/A	0.21	0.04
I28	2.62	325.03	36.13	0.73	0.54	17.14	2.59	16.30	0.45	0.25	0.31	0.06
S29	2.44	30.78	27.07	0.88	0.66	17.71	3.05	16.68	0.44	0.24	0.42	0.13
S29	2.44	30.80	26.24	0.85	0.55	17.79	2.82	16.77	0.44	0.24	0.37	0.12
P35	2.52	316.27	-2.71	0.58	0.36	13.96	2.02	13.18	0.50	0.26	0.26	0.09
P35	2.52	317.88	1.48	0.61	0.48	14.48	2.34	13.83	0.44	0.23	0.17	0.06
T1	3.80	18.17	3.97	0.80	0.60	16.43	1.34	14.97	N/A	N/A	N/A	N/A
T1	3.80	19.29	0.79	0.86	0.47	18.06	1.45	16.46	0.45	0.24	N/A	N/A
T3	3.75	28.02	-2.68	0.63	0.42	17.30	1.64	15.95	0.51	0.27	0.15	0.04
T3	3.75	30.12	-1.90	0.53	0.35	17.78	1.69	16.38	0.46	0.26	0.18	0.08
T2	3.76	28.16	15.48	0.82	0.54	15.07	0.43	13.41	0.68	0.35	0.22	0.08
T4	3.75	30.42	14.27	0.85	0.56	17.78	1.60	15.97	0.48	0.25	0.25	0.05

Mare	Age	Long	Lat	Topographic Roughness	St Dev TR	Pulse Width	St Dev PW	Slope Corrected PW	S CPR	St Dev S CPR	P CPR	St Dev P CPR
S1	3.81	30.20	22.01	N/A	N/A	N/A	N/A	N/A	0.74*	0.39*	0.40	0.12
S2	3.76	10.31	20.12	0.56	0.29	17.56	2.42	15.85	0.54*	0.30*	0.14	0.03

Appendix C. Table of roughness data for mare flows of varying ages. Unit names (P60, S2, etc.) follow those defined by Hiesinger et al. (2000; 2003; 2010) and are outlined in white in Figure 13. Age values are in Ga; all other units are the same as in Appendix B. N/A indicates no data in a particular parameter for a given feature. * Starred values may have been affected by edge brightening in the radar data.

References

Besse, S., Sunshine, J. M., Staid, M. I., Petro, N. E., Boardman, J. W., Green, R. O., Head, J. W., Isaacson, J. F., Mustard, J. F., and Pieters, C. M. (2011). Compositional variability of the Marius Hills volcanic complex from the Moon Mineralogy Mapper (M^3). *Journal of Geophysical Research*, 116(E00G13), doi:10.1029/2010JE003725

Bart, G. D. & Melosh, H. J. (2010). Distributions of boulders ejected from lunar craters. *Icarus*, 209, 337-357, doi:10.1016/j.icarus.2010.05.023

Bogard, D. D., Garrison, D. H., Shih, C. Y., and Nyquist, L. E. (1994). AR-39-AR-40 Dating of 2 Lunar Granites – The Age of Copernicus. *Geochimica et Cosmochimica Acta*, 58(14), 3093-3100, doi:10.1016/0016-7037(94)90181-3

Campbell, B. A., Carter, L. M., Hawke, B. R., Campbell, D. B., and Ghent, R. R. (2008). Volcanic and impact deposits of the Moon's Aristarchus Plateau: A new view from Earth-based radar images. *Geology*, 36(2), 135-138, doi:10.1130/G24310A.1

Campbell, B. A., Hawke, B. R., and Campbell, D. B. (2009b). Surface morphology of domes in the Marius Hills and Mons Rümker regions of the Moon from Earth-based radar data. *Journal of Geophysical Research*, 114(E01001), doi:10.1029/2008JE003253

Campbell, B. A., Hawke, B. R., Carter, L. M., Ghent, R. R., and Campbell, D. B. (2009a). Rugged lava flows on the Moon revealed by Earth-based radar. *Geophysical Research Letters*, 36(L22201), doi:10.1029/2009GL041087

Campbell, B. A. & Shepard, M. K. (1996). Lava flow surface roughness and depolarized radar scattering. *Journal of Geophysical Research*, 101(E8), 18,941-18,951.

Carter, L. M., Campbell, B. A., Hawke, B. R., Campbell, D. B., and Nolan,

M. C. (2009). Radar remote sensing of pyroclastic deposits in the southern Mare Serenitatis and Mare Vaporum regions of the Moon. *Journal of Geophysical Research*, 114(E11004), doi:10.1029/2009JE003406

Dhingra, D. & Pieters, C. M. (2011). MG-Spinel Rich Lithology at Crater Copernicus. Presented at the Annual meeting of the Lunar Exploration Analysis Group, Houston, TX. Abs. No. 2024.

Dundas, C. M. & McEwen, A. S. (2007). Rays and secondary craters of Tycho. *Icarus*, 186, 31-40, doi:10.1016/j.icarus.2006.08.11

Eberhardt, P., Geiss, J., Grögler, N., and Settler, A. (1972). How Old is the Crater Copernicus? *The Moon*, 8, 104-114.

Gaddis, L. R., Mouginis-Mark, P., Singer, R., and Kaupp, V. (1989). Geologic analyses of Shuttle Imaging Radar (SIR-B) data of Kilauea Volcano, Hawaii. *GSA Bulletin*, 101, 317-332.

Gaddis, L. R., Mouginis-Mark, P. J., and Hayashi, J. N. (1990). Lava Flow Surface Textures: SIR-B Radar Image Texture, Field Observations, and Terrain Measurements. *Photogrammetric Engineering and Remote Sensing*, 56(2), 211-224.

Galilei, G. (1957). *Discoveries and Opinions of Galileo*. S. Drake, (Ed.). Garden City, NY: Anchor.

Glotch, T. D., Lucey, P. G., Bandfield, J. L., Greenhagen, B. T., Thomas, I. R., Elphic, R. C., Bowles, N., Wyatt, M. B., Allen, C. C., Hanna, K. D., and Paige, D. A. (2010). Highly Silicic Compositions on the Moon. *Science*, 329 (1510), doi:10.1126/science.1192148

Hawke, B. R., Blewett, D. T., Lucey, P. G., Smith, G. A., Bell, J. F., Campbell, B. A., and Robinson, M. S. (2004). The origin of lunar crater rays. *Icarus*, 170, 1-16, doi:10.1016/j.icarus.2004.02.013

Head, J. W. (1974). Lunar dark-mantle deposits: Possible clues to the distribution of early mantle deposits. Proceedings of the Lunar and

Planetary Sciences Conference 5, Houston, TX.

Hiesinger, H., Jaumann, R., Neukum, G., and Head, J. W. (2000). Ages of mare basalts on the lunar nearside. *Journal of Geophysical Research*, 105(E12), 29,239-29,275.

Hiesinger, H., Head, J. W., Wolf, U., Jaumann, R., and Neukum, G. (2003). Ages and stratigraphy of mare basalts in Oceanus Procellarum, Mare Nubium, Mare Cognitum, and Mare Insularum. *Journal of Geophysical Research*, 108(E7), doi:10.1029/2002JE001985

Hiesinger, H., Head, J. W., Wolf, U., Jaumann, R., and Neukum, G. (2010). Ages and stratigraphy of lunar mare basalts in Mare Frigoris and other nearside maria based on crater size-frequency distribution measurements. *Journal of Geophysical Research*, 115(E03003), doi:10.1029/2009JE003380

Langevin, Y. & Arnold, J.R. (1977). The Evolution of the Lunar Regolith. *Annual Review of Earth and Planetary Sciences*, 5, 449-489.

Liu, F., Yang, R., Zhang, Y., Qiao, L., Wang, S., Yang, Y., and Wang, X. (2011). Distribution of Olivine and Pyroxene Derived from Clementine Data in Crater Copernicus. *Journal of Earth Science*, 22(5), 586-594, doi:10.1007/s12583-011-0209-2

Melosh, J. (1989). *Impact Cratering: A Geologic Process*. New York: Oxford University Press.

Neumann, G. A., Abshire, J. B., Aharonson, O., Garvin, J. B., Sun, X., and Zuber, M. T. (2003). Mars Orbiter Laser Altimeter pulse width measurements and footprint-scale roughness. *Geophysical Research Letters*, 30(11), doi: 10.1029/2003GL017048

Neumann, G. A., Smith, D. E., Zuber, M. T., Mazarico, E., Torrence, M. H., Cavanaugh, J. C., and LOLA Science Team (2009). Meter-scale Roughness on the Moon from Lunar Orbiter Laser Altimeter (LOLA) Pulse Spreading: Implications for Exploration. Presented at the annual

meeting of the Lunar Exploration Analysis Group, Houston, TX. Abs. No. 2047.

Nozette, S., Spudis, P., Bussey, B., Jensen, R., Raney, K., Winters, H., Lichtenberg, C. L., Marinelli, W., Crusan, J., Gates, M., and Robinson, M. (2010). The Lunar Reconnaissance Orbiter Miniature Radio Frequency (Mini-RF) Technology Demonstration. *Space Science Reviews*, 150, 285-302, doi:10.1007/s11214-009-9607-5

Pettengill, G. H. & Thompson, T. W. (1968). A Radar Study of the Lunar Crater Tycho at 3.8-cm and 70-cm Wavelengths. *Icarus*, 8, 457-471, doi:10.1016/0019-1035(68)90092-4

Pieters, C. (1982). Copernicus Central Peak: Lunar Mountain of Unique Composition. *Science*, 215(4528), 59-61.

Plaut, J. J., Anderson, S. W., Crown, D. A., Stofan, E. R., and van Zyl, J. J. (2004). The unique radar properties of silicic lava domes. *Journal of Geophysical Research*, 109(E03001), doi:10.1029/2002JE002017

Prettyman, T. H., Hagerty, J. J., Elphic, R. C., Feldman, W. C., Lawrence, D. J., McKinney, G. W., and Vaniman, D. T. (2006). Elemental composition of the lunar surface: Analysis of gamma ray spectroscopy data from Lunar Prospector. *Journal of Geophysical Research*, 111(E12007), doi:10.1029/2005JE002656

Raney, K., Spudis, P. D., Bussey, B., Crusan, J., Jensen, J. R., Marinelli, W., McKerracher, P., Neish, C., Palsetia, M., Schulze, R., Sequeira, H. B., and Winters, H. (2010). The Lunar Mini-RF Radars: Hybrid Polarimetric Architecture and Initial Results. *Proceedings of the IEEE*, 99(5), 808-823, doi:10.1109/JPROC.2010.2084970

Rosenburg, M. A., Aharonson, O., Head, J. W., Kreslavsky, M. A., Mazarico, E., Neumann, G. A., Smith, D. E., Torrence, M. H., and Zuber, M. T. (2011). Global surface slopes and roughness of the Moon from the Lunar Orbiter Laser Altimeter. *Journal of Geophysical Research*, 116(E02001), doi: 10.1029/2010JE003716

Smith, D. E., Zuber, M. T., Frey, H. V., Garvin, J. B., Head, J. W., Muhleman, D. O., Pettengill, G. H., Phillips, R. J., Solomon, S. C., Zwally, H. J., Banerdt, W. B., Duxbury, T. C., Golombek, M. P., Lemoine, F. G., Neumann, G. A., Rowlands, D. D., Aharonson, O., Ford, P. G., Ivanov, A. B., Johnson, C. L., McGovern, P. J., Abshire, J. B., Afzal, R. S., and Sun, X. (2001). Mars Orbiter Laser Altimeter: Experiment summary after the first year of global mapping of Mars. *Journal of Geophysical Research*, 106(E10), 23,689-23,722.

Smith, D. E., Zuber, M. T., Jackson, G. B., Cavanaugh, J. F., Neumann, G. A., Riris, H., Sun, X., Zellar, R. S., Coltharp, C., Connelly, J., Katz, R. B., Kleyner, I., Liiva, P., Matuszeski, A., Mazarico, E. M., McGarry, J. F., Novo-Gradac, A., Ott, M. N., Pieters, C., Ramos-Izquierdo, L. A., Ramsey, L., Rowlands, D. D., Schmidt, S., Scott, V. S., Shaw, G. B., Smith, J. C., Swinski, J., Torrence, M. H., Unger, G., Yu, A. W., and Zagwodzki, T. W. (2010b). The Lunar Orbiter Laser Altimeter Investigation on the Lunar Reconnaissance Orbiter. *Space Science Reviews*, 150, 209-241, doi:10.1007/s11214-009-9512-y

Smith, D. E., Zuber, M. T., Neumann, G. A., Lemoine, F. G., Mazarico, E., Torrence, M. H., McGarry, J. F., Rowlands, D. D., Head, J. W., Duxbury, T. H., Aharonson, O., Lucey, P. G., Robinson, M. S., Barnouin, O. S., Cavanaugh, J. F., Sun, X., Liiva, P., Mao, D., Smith, J. C., and Bartels, A. E. (2010a). Initial observations from the Lunar Orbiter Laser Altimeter (LOLA). *Geophysical Research Letters*, 37(L18204), doi:10.1029/2010GL043751

Spudis, P., Nozette, S., Bussey, B., Raney, K., Winters, H., Lichtenberg, C. L., Marinelli, W., Crusan, J. C., and Gates, M. M. (2009). Mini-SAR: an imaging radar experiment for the Chandrayaan-1 mission to the Moon. *Current Science*, 96(4), 533-539.

Stöffler, D. & Ryder, G. (2001). Stratigraphy and isotope ages of lunar geologic units: Chronological standard for the inner solar system. *Space Science Reviews*, 96, 9-54.

Sunshine, J. M., Pieters, C. M., and Head, J. W. (1994). New Evidence for Compositional Diversity on the Marius Hills Plateau from *Galileo* Multi Spectral Imaging. Presented at the annual meeting of the Lunar and Planetary Sciences Conference XXV, Houston, TX.

Torson, J. M. & Becker, K. J. (1997). ISIS – A Software Architecture for Processing Planetary Images. Presented at the annual meeting of the Lunar and Planetary Sciences Conference, Houston, TX, pp. 1443-1444.

Weitz, C. M. & Head, J. W. (1999). Spectral Properties of the Marius Hills volcanic complex and implications for the formation of lunar domes and cones. *Journal of Geophysical Research*, 104(E8), 18,933-18,956.

Wilson, L. & Head, J. W. (2003). Lunar Gruithuisen and Mairan domes: Rheology and mode of emplacement. *Journal of Geophysical Research*, 108(E2), doi:10.1029/2002JE001909

Yamamoto, S., Nakamura, R., Matsunaga, T., Ogawa, Y., Ishihara, Y., Morota, T., Hirata, N., Ohtake, M., Hiroi, T., Yokota, Y., and Haruyama, J. (2010). Possible mantle origin of olivine around lunar impact basins detected by SELENE. *Nature Geoscience*, 2, 533-536, doi:10.1038/ngeo897